Spatially Fixed and Moving Virtual Sensing Methods for Active Noise Control

Danielle J. Moreau

School of Mechanical Engineering
The University of Adelaide
South Australia 5005
Australia

A thesis submitted in fulfillment of the requirements
for the degree of Ph.D. in Mechanical Engineering
on 11 December 2009. Qualified on 12 February 2010.

Chapter 4

Moving Virtual Microphone Methods in a Three-dimensional Sound Field

The spatially fixed virtual sensing algorithms presented in Chapters 2 and 3 can be used to shift the zone of quiet to a desired location that is remote from the physical error sensor. While significant attenuation may be achieved at the virtual location with these virtual sensing algorithms, the spatial extent of the zone of quiet is still impractically small. Large pressure gradients in the vicinity of the virtual sensor result in significant changes in the perceived sound pressure level as the observer moves around within the zone of quiet and this could be more annoying than the original disturbance alone. Consequently, Petersen et al. (2006, 2007) and Petersen (2007) developed a number of one-dimensional moving virtual sensing algorithms that create a zone of quiet capable of tracking a moving virtual location in a one-dimensional sound field. Hence if the observer moves their head, the small zone of quiet also moves with the observer. The one-dimensional moving virtual sensing algorithms developed by Petersen et al. (2006, 2007) and Petersen (2007) use the remote microphone technique (Roure and Albarrazin, 1999), the adaptive LMS virtual microphone technique (Cazzolato, 2002) and the Kalman filtering virtual sensing method (Petersen et al., 2008). Details of these one-dimensional moving virtual sensing algorithms have been given in Chapter 2.

In this chapter, a number of moving virtual sensing methods are presented for use in three-dimensional sound fields. These moving virtual sensing algorithms create a zone of quiet capable of tracking a three-dimensional trajectory in a three-

dimensional sound field. The moving virtual sensing algorithms developed here employ the remote microphone technique (Roure and Albarrazin, 1999), the adaptive LMS virtual microphone technique (Cazzolato, 2002) and the stochastically optimal tonal diffuse field (SOTDF) virtual sensing method developed in Chapter 3 to estimate the virtual error signal at the moving virtual location. To determine the level of attenuation that can be expected at the ear of a human observer in practice, the performance of these moving virtual sensing algorithms in generating a moving zone of quiet at a single ear of a rotating artificial head is experimentally investigated in a modally dense three-dimensional cavity. As in previous research (Petersen et al., 2006, Petersen et al., 2007, Petersen, 2007), it is assumed that an exact measurement of the moving virtual location is available. In practical applications, the moving virtual location can be measured using a 3D head tracking system based on camera vision or on ultrasonic position sensing such as the Logitech Head Tracker (Petersen et al., 2007). To create a zone of quiet at the ear of the rotating artificial head in real-time, the moving virtual sensing algorithms are combined with a modified version of the filtered-x LMS algorithm. A modified version of the filtered-x LMS algorithm is used to account for the fact that the virtual location is moving through the sound field.

The SOTDF moving virtual sensing method developed in this chapter employs the SOTDF virtual sensing method to obtain an estimate of the error signal at the moving virtual location. The performance of SOTDF virtual sensors has been numerically and experimentally investigated in a pure tone diffuse sound field in Chapter 3 and results indicate that this virtual sensing method performs as predicted by diffuse field theory. In many real world applications however, it is likely that the sound field is not perfectly diffuse. In this chapter, the performance of SOTDF moving virtual microphones is experimentally investigated in a modally dense three-dimensional cavity. The experimental results presented here therefore demonstrate the performance of the SOTDF virtual sensing method in a sound field that is not perfectly diffuse.

Section 4.1 presents a derivation of each of the moving virtual sensing algorithms. The experimental method including a discussion of the modified filtered-x LMS algorithm for real-time control is detailed in Section 4.2. Finally, results of real-time experiments of the creation of a moving zone of quiet at a virtual sensor located at a single ear of a rotating artificial head are discussed in Section 4.3.

4.1 Theoretical background

This section presents the moving virtual sensing algorithms for generating a moving virtual microphone capable of tracking a three-dimensional trajectory in a three-dimensional sound field. The moving virtual sensing algorithms based on the remote microphone technique, the adaptive LMS virtual microphone technique and the SOTDF virtual sensing method are presented as follows.

4.1.1 The remote moving microphone technique for a three-dimensional sound field

The remote moving microphone technique for a three-dimensional sound field uses the remote microphone technique (Roure and Albarrazin, 1999) to generate a moving virtual microphone that tracks a three-dimensional trajectory. Generating a moving zone of quiet that tracks a three-dimensional trajectory in a three-dimensional sound field requires a single secondary source, a single physical microphone and a single moving virtual microphone. The time-varying location of the moving virtual microphone is defined by three spatial co-ordinates with respect to a reference frame and is given by

$$\mathbf{x}_v(n) = \left[\begin{array}{ccc} x_v(n) & y_v(n) & z_v(n) \end{array} \right]^{\mathrm{T}}. \tag{4.1}$$

As the moving virtual location, $\mathbf{x}_v(n)$, follows a three-dimensional trajectory through the three-dimensional sound field, each of the three spatial co-ordinates are time-varying. It is assumed here that the moving virtual location, $\mathbf{x}_v(n)$, is known at every time step.

A block diagram of the remote moving microphone technique for a three-dimensional sound field is given in Fig. 4.1. In this moving virtual sensing algorithm, the remote microphone technique is first used to obtain estimates of the virtual error signals, $\tilde{\bar{\mathbf{p}}}_v(n)$, at $\bar{M}_v$ spatially fixed virtual microphone locations, $\bar{\mathbf{x}}_v$. It is assumed here that the moving virtual location, $\mathbf{x}_v(n)$, is confined to a certain three-dimensional region and that the spatially fixed virtual microphone locations, $\bar{\mathbf{x}}_v$, are therefore located within this three-dimensional region. The vector of the $\bar{M}_v$ spatially fixed virtual microphone locations is given by

$$\bar{\mathbf{x}}_v = \left[\begin{array}{cccc} \bar{\mathbf{x}}_{v1} & \bar{\mathbf{x}}_{v2} & \ldots & \bar{\mathbf{x}}_{v\bar{M}_v} \end{array} \right], \tag{4.2}$$

where each of the spatially fixed virtual locations, $\bar{\mathbf{x}}_{v\bar{m}_v}$, are defined by three spatial

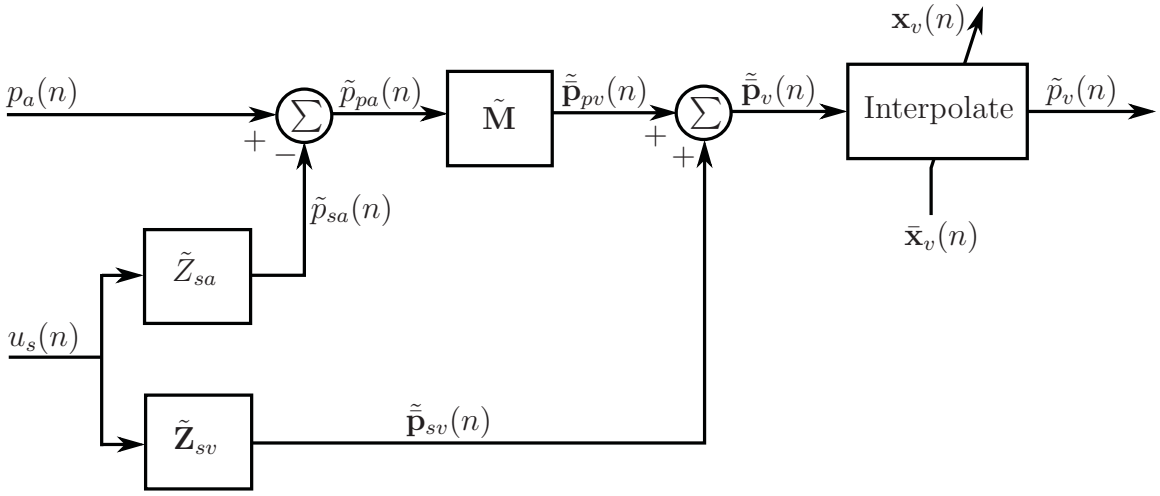

Figure 4.1: Block diagram of the remote moving microphone technique for a three-dimensional sound field.

co-ordinates with respect to a reference frame and are given by

$$\bar{\mathbf{x}}_{v\bar{m}_v} = \left[\begin{array}{ccc} \bar{x}_{v\bar{m}_v} & \bar{y}_{v\bar{m}_v} & \bar{z}_{v\bar{m}_v} \end{array} \right]^{\mathrm{T}}. \tag{4.3}$$

The virtual error signals, $\tilde{\bar{\mathbf{p}}}_v(n)$, at the spatially fixed virtual locations, $\bar{\mathbf{x}}_v$, are calculated using the remote microphone technique as described in Section 2.1.3. A preliminary identification stage is first required in which the physical secondary transfer function $\tilde{Z}_{sa}$ and the $\bar{M}_v$ virtual secondary transfer functions, $\tilde{\mathbf{Z}}_{sv}$, are modelled as FIR or IIR filters. The vector of the $\bar{M}_v$ primary transfer functions at the spatially fixed virtual locations from the physical location, $\tilde{\mathbf{M}}$, is also estimated as a vector of FIR or IIR filters during this preliminary identification stage.

An estimate of the primary disturbance, $\tilde{p}_{pa}(n)$, at the physical microphone is first calculated using

$$\tilde{p}_{pa}(n) = p_a(n) - \tilde{p}_{sa}(n) = p_a(n) - \tilde{Z}_{sa}u_s(n). \tag{4.4}$$

Next, estimates of the primary disturbances, $\tilde{\bar{\mathbf{p}}}_{pv}(n)$, at the spatially fixed virtual locations, $\bar{\mathbf{x}}_v$, are found to be

$$\tilde{\bar{\mathbf{p}}}_{pv}(n) = \tilde{\mathbf{M}}\tilde{p}_{pa}(n). \tag{4.5}$$

Estimates, $\tilde{\bar{\mathbf{p}}}_v(n)$, of the total virtual error signals at the spatially fixed virtual

locations, $\bar{\mathbf{x}}_v$, are calculated as

$$\tilde{\bar{\mathbf{p}}}_v(n) = \tilde{\bar{\mathbf{p}}}_{pv}(n) + \tilde{\bar{\mathbf{p}}}_{sv}(n) = \tilde{\mathbf{M}}\tilde{p}_{pa}(n) + \tilde{\mathbf{Z}}_{sv}u_s(n). \tag{4.6}$$

An estimate, $\tilde{p}_v(n)$, of the virtual error signal at the moving virtual location, $\mathbf{x}_v(n)$, is now obtained by interpolating the virtual error signals, $\tilde{\bar{\mathbf{p}}}_v(n)$, at the spatially fixed virtual locations, $\bar{\mathbf{x}}_v$, over three-dimensions.

As the virtual error signal at the moving virtual location, $\tilde{p}_v(n)$, is estimated by interpolating the virtual error signals, $\tilde{\bar{\mathbf{p}}}_v(n)$, at $\bar{M}_v$ spatially fixed virtual microphone locations, the accuracy of the estimate is dependent on the number and position of the spatially fixed measurement locations within the sound field. If the sound field varies significantly in magnitude and phase over a certain region then the spatially fixed measurement locations must be closely spaced within this region to ensure an accurate estimate of the moving virtual error signal is obtained.

4.1.2 The adaptive LMS moving virtual microphone technique for a three-dimensional sound field

The adaptive LMS moving virtual microphone technique for a three-dimensional sound field uses the adaptive LMS virtual microphone technique (Cazzolato, 2002) to generate a moving virtual microphone that tracks a three-dimensional trajectory. A block diagram of the adaptive LMS moving virtual microphone technique for a three-dimensional sound field is given in Fig. 4.2. This moving virtual sensing technique is used to compute an estimate of the virtual error signal, $\tilde{p}_v(n)$, at the moving virtual location, $\mathbf{x}_v(n)$, defined in Eq. (4.1). It employs the adaptive LMS algorithm to adapt the weights of M_a physical microphones in an array so that the weighted summation of these signals minimises the mean square difference between the predicted and measured pressure at the $\bar{M}_v$ spatially fixed virtual locations, $\bar{\mathbf{x}}_v$. It is worth noting that multiple virtual sensors can be generated simultaneously from the same array of physical microphones.

As shown in Fig. 4.2, the primary component of the physical error signals is calculated using the vector of physical secondary transfer functions $\tilde{\mathbf{Z}}_{sa}$ and is given as

$$\tilde{\mathbf{p}}_{pa}(n) = \mathbf{p}_a(n) - \tilde{\mathbf{p}}_{sa}(n) = \mathbf{p}_a(n) - \tilde{\mathbf{Z}}_{sa}u_s(n). \tag{4.7}$$

The physical secondary transfer function vector $\tilde{\mathbf{Z}}_{sa}$ is estimated as a vector of FIR or IIR filters during a preliminary identification stage. Also during this preliminary

identification stage, matrices of the primary and secondary weights, $\mathbf{w}_p$ and $\mathbf{w}_s$, of size $M_a \times \bar{M}_v$, at the $\bar{M}_v$ spatially fixed virtual locations are estimated separately using the adaptive LMS algorithm. As only a single temporal tap is used, the real valued weights correspond to pure gain and are calculated using

$$\mathbf{w}_p(n+1) = \mathbf{w}_p(n) + 2\mu \mathbf{p}_{pa}(n)\epsilon_p(n), \tag{4.8}$$

$$\mathbf{w}_s(n+1) = \mathbf{w}_s(n) + 2\mu \mathbf{p}_{sa}(n)\epsilon_s(n), \tag{4.9}$$

where μ is the convergence coefficient and $\epsilon_p(n)$ and $\epsilon_s(n)$ are the primary and secondary error terms respectively. The primary error term, $\epsilon_p(n)$, is defined as the difference between the actual and estimated virtual primary disturbance at the $\bar{M}_v$ spatially fixed virtual locations, $\bar{\mathbf{x}}_v$, and is given by

$$\epsilon_p(n) = \bar{\mathbf{p}}_{pv}(n) - \tilde{\bar{\mathbf{p}}}_{pv}(n), \tag{4.10}$$

where the estimated virtual primary disturbance at the $\bar{M}_v$ spatially fixed virtual locations, $\bar{\mathbf{x}}_v$, is given by

$$\tilde{\bar{\mathbf{p}}}_{pv}(n) = \mathbf{w}_p^{\mathrm{T}} \mathbf{p}_{pa}(n). \tag{4.11}$$

Similarly, the secondary error term, $\epsilon_s(n)$, is defined as the difference between the actual and estimated virtual secondary disturbance at the $\bar{M}_v$ spatially fixed virtual locations, $\bar{\mathbf{x}}_v$, and is given by

$$\epsilon_s(n) = \bar{\mathbf{p}}_{sv}(n) - \tilde{\bar{\mathbf{p}}}_{sv}(n), \tag{4.12}$$

where the estimated virtual secondary disturbance at the $\bar{M}_v$ spatially fixed virtual locations, $\bar{\mathbf{x}}_v$, is given by

$$\tilde{\bar{\mathbf{p}}}_{sv}(n) = \mathbf{w}_s^{\mathrm{T}} \mathbf{p}_{sa}(n). \tag{4.13}$$

Estimates, $\tilde{\bar{\mathbf{p}}}_v(n)$, of the total virtual error signals at the spatially fixed virtual locations, $\bar{\mathbf{x}}_v$, can then be calculated as

$$\tilde{\bar{\mathbf{p}}}_v(n) = \tilde{\bar{\mathbf{p}}}_{pv}(n) + \tilde{\bar{\mathbf{p}}}_{sv}(n) = \mathbf{w}_p^{\mathrm{T}} \tilde{\mathbf{p}}_{pa}(n) + \mathbf{w}_s^{\mathrm{T}} \tilde{\mathbf{p}}_{sa}(n). \tag{4.14}$$

An estimate, $\tilde{p}_v(n)$, of the virtual error signal at the moving virtual location, $\mathbf{x}_v(n)$, is now obtained by interpolating the virtual error signals, $\tilde{\bar{\mathbf{p}}}_v(n)$, at the spatially fixed virtual locations, $\bar{\mathbf{x}}_v$, over three-dimensions.

Similarly to the remote moving microphone technique for a three-dimensional

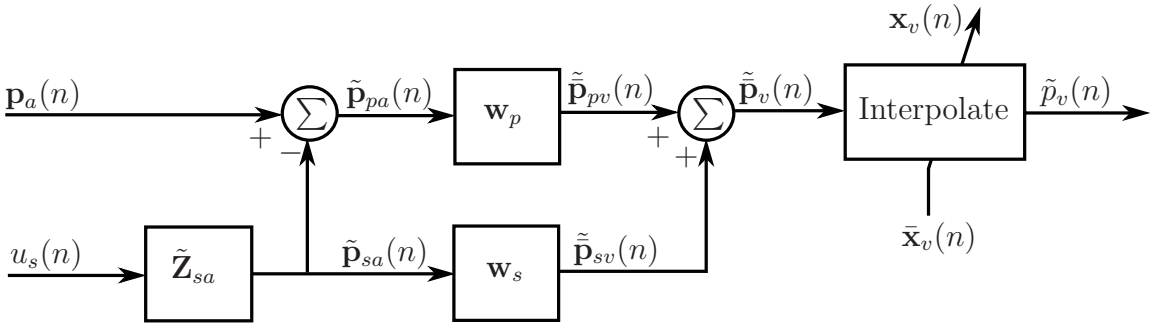

Figure 4.2: Block diagram of the adaptive LMS moving virtual microphone technique for a three-dimensional sound field.

sound field, the virtual error signal at the moving virtual location, $\tilde{p}_v(n)$, is obtained by interpolating the virtual error signals, $\tilde{\bar{\mathbf{p}}}_v(n)$, at the $\bar{M}_v$ spatially fixed virtual microphone locations with this moving virtual sensing method. Therefore the accuracy of the estimate of the moving virtual error signal is dependent on the number and position of the spatially fixed measurement locations within the sound field. Again, if the sound field varies significantly in magnitude and phase over a certain region then the spatially fixed measurement locations must be closely spaced within this region to ensure an accurate estimate of the moving virtual error signal is obtained.

4.1.3 The Stochastically Optimal Tonal Diffuse Field (SOTDF) moving virtual sensing method for a three-dimensional sound field

The SOTDF moving virtual sensing method generates a stochastically optimal moving virtual microphone that tracks a three-dimensional trajectory in a three-dimensional sound field. This moving virtual sensing method is derived using the SOTDF virtual sensing method presented in Chapter 3. Stochastically optimal moving virtual microphones are developed using control strategy 6 (estimating the pressure at a virtual location using the pressure and pressure gradient at a point) and control strategy 7 (estimating the pressure at a virtual location using the pressures at two points). For comparison, in this chapter a SOTDF moving virtual microphone is also developed using the measured pressures at three points to estimate the moving virtual error signal. This control strategy is investigated to determine if increasing the number of physical error sensors results in a more accurate estimate of the error signal at the moving virtual location.

The SOTDF moving virtual sensing method is a fixed scalar weighting method requiring only sensor position information. Unlike the remote moving microphone technique or the adaptive LMS moving virtual microphone technique, this moving virtual sensing method does not require a preliminary identification stage nor FIR filters or similar to model the complex transfer functions between the error sensors and the sources. As such, this prediction technique is robust to physical system changes that alter the transfer functions between the error sensors and secondary sources.

Slightly different notation from the previous sections will be adopted in the following to highlight the dependence on position.

4.1.3.1 Estimating the pressure at a moving virtual location using the measured pressure and pressure gradient at a point

Firstly the error signal at the moving virtual location $\tilde{p}_v(\mathbf{x}_v(n))$, is estimated using the measured pressure, $p(\mathbf{x}_1)$, and pressure gradient, $g(\mathbf{x}_1)$, at a position $\mathbf{x}_1$. A stochastically optimal estimate of the pressure at the virtual location using the measured pressure and pressure gradient at a point has been derived in Section 3.1.6 and is given in Eq. (3.67). This estimate of the pressure at the virtual location only requires that the distance between the virtual and physical sensors is known. From Eq. (3.67) it follows that a stochastically optimal estimate of the pressure at the moving virtual location, $\mathbf{x}_v(n)$, using the measured pressure and pressure gradient at a point, is given by

$$\tilde{p}_v(\mathbf{x}_v(n)) \;=\; A(\mathbf{x}_v(n)-\mathbf{x}_1)p(\mathbf{x}_1) - \frac{3}{k^2}B(\mathbf{x}_v(n)-\mathbf{x}_1)g(\mathbf{x}_1), \qquad (4.15)$$

where $A(\mathbf{x}_v(n)-\mathbf{x}_1)$ and $B(\mathbf{x}_v(n)-\mathbf{x}_1)$ are found using Eqs. (3.1) and (3.2).

The accuracy of the pressure estimate at the moving virtual location depends on the distance between the physical and virtual sensors. As this distance increases, the pressure at the virtual location and the measured quantities become uncorrelated and the optimal pressure estimate given by Eq. (4.15) approaches zero. If none of the distances between the virtual location and the physical sensors are small, then the pressure at the virtual location will be uncorrelated with the measured quantities and the best estimate of the pressure will be close to zero.

An expression for the relative change in mean squared pressure at a point, $\mathbf{x}$, when a single secondary source is used to cancel the pressure at a virtual location estimated using the pressure and pressure gradient at a point, has been given in

Eq. (3.78). This expression can be modified such that when the pressure at a moving virtual location, $\mathbf{x}_v(n)$, is minimised with a single secondary source, the relative change in mean squared pressure at a point, $\mathbf{x}$, in the controlled sound field is given by

$$\frac{\left\langle |p(\mathbf{x})|^2 \right\rangle}{\left\langle |p_p|^2 \right\rangle} = \left(1 - \frac{\left(A(\mathbf{x}_v(n) - \mathbf{x}_1) A(\mathbf{x} - \mathbf{x}_1) + \frac{3}{\mathrm{k}^2} B(\mathbf{x}_v(n) - \mathbf{x}_1) B(\mathbf{x} - \mathbf{x}_1) \right)^2}{A^2(\mathbf{x}_v(n) - \mathbf{x}_1) + \frac{3}{k^2} B^2(\mathbf{x}_v(n) - \mathbf{x}_1)} \right) \alpha, \tag{4.16}$$

where α is the increase in the mean squared pressure of the acoustic field after control.

4.1.3.2 Estimating the pressure at a moving virtual location using the measured pressures at two points

In this case, the pressure at the moving virtual location, $\tilde{p}_v(\mathbf{x}_v(n))$, is estimated using the measured pressures, $p(\mathbf{x}_1)$ and $p(\mathbf{x}_2)$, at two points, $\mathbf{x}_1$ and $\mathbf{x}_2$. A stochastically optimal estimate of the pressure at the virtual location using the measured pressures at two points has been derived in Section 3.1.7 and is given in Eq. (3.83). Again, this estimate of the pressure at the virtual location only requires that the distance between the virtual and physical sensors is known. From Eq. (3.83) it follows that a stochastically optimal estimate of the pressures at the moving virtual location, $\mathbf{x}_v(n)$, using the measured pressures at two points, is given by

$$\begin{aligned} \tilde{p}_v(\mathbf{x}_v(n)) &= \frac{A(\mathbf{x}_v(n) - \mathbf{x}_1) - A(\mathbf{x}_1 - \mathbf{x}_2) A(\mathbf{x}_v(n) - \mathbf{x}_2)}{1 - A(\mathbf{x}_1 - \mathbf{x}_2)^2} p(\mathbf{x}_1) \\ &+ \frac{A(\mathbf{x}_v(n) - \mathbf{x}_2) - A(\mathbf{x}_1 - \mathbf{x}_2) A(\mathbf{x}_v(n) - \mathbf{x}_1)}{1 - A(\mathbf{x}_1 - \mathbf{x}_2)^2} p(\mathbf{x}_2). \end{aligned} \tag{4.17}$$

As mentioned previously, the accuracy of the pressure estimate at the moving virtual location depends on the distance between the physical and virtual sensors. As this distance increases, the pressure at the virtual location and the measured quantities become uncorrelated and the pressure estimate given by Eq. (4.17) approaches zero.

An expression for the relative change in mean squared pressure at a point, $\mathbf{x}$, when a single secondary source is used to cancel the pressure at a virtual location estimated using the pressures at two points, has been given in Eq. (3.93). This expression can be modified such that when the pressure at a single moving virtual location, $\mathbf{x}_v(n)$, is minimised with a single secondary source, the relative change in

mean squared pressure at a point, $\mathbf{x}$, in the controlled sound field is given by

$$\frac{\left\langle |p(\mathbf{x})|^2 \right\rangle}{\left\langle |p_p|^2 \right\rangle} = \left(1 - \frac{\left(A_1(n)A(\mathbf{x}-\mathbf{x}_1) + A_2(n)A(\mathbf{x}-\mathbf{x}_2) \right)^2}{A_1^2(n) + A_2^2(n) + 2A_1(n)A_2(n)A(\mathbf{x}_1-\mathbf{x}_2)} \right) \alpha, \tag{4.18}$$

where $A_1(n)$ and $A_2(n)$ are given by

$$A_1(n) = \frac{A(\mathbf{x}_v(n)-\mathbf{x}_1) - A(\mathbf{x}_1-\mathbf{x}_2)A(\mathbf{x}_v(n)-\mathbf{x}_2)}{1 - A(\mathbf{x}_1-\mathbf{x}_2)^2}, \tag{4.19}$$

$$A_2(n) = \frac{A(\mathbf{x}_v(n)-\mathbf{x}_2) - A(\mathbf{x}_1-\mathbf{x}_2)A(\mathbf{x}_v(n)-\mathbf{x}_1)}{1 - A(\mathbf{x}_1-\mathbf{x}_2)^2}, \tag{4.20}$$

and α is the increase in the mean squared pressure of the acoustic field after control.

4.1.3.3 Estimating the pressure at a moving virtual location using the measured pressures at three points

Finally, the pressure at the moving virtual location, $\tilde{p}_v(\mathbf{x}_v(n))$, is estimated using the measured pressures, $p(\mathbf{x}_1)$, $p(\mathbf{x}_2)$ and $p(\mathbf{x}_3)$, at three points, $\mathbf{x}_1$, $\mathbf{x}_2$ and $\mathbf{x}_3$. A stochastically optimal estimate of the pressure at the moving virtual location using the measured pressures at three points can be derived using the procedure outlined in Section 3.1.6. In this case, the matrix of $\mathbf{p}$, whose elements are the pressures measured at the sensors, is given by

$$\mathbf{p} = \begin{bmatrix} p(\mathbf{x}_1) \\ p(\mathbf{x}_2) \\ p(\mathbf{x}_3) \end{bmatrix}. \tag{4.21}$$

It was shown in Section 3.1.6 that the best estimate of the pressure at a spatially fixed virtual location, $\mathbf{x}_0$, is

$$\tilde{p_v}(\mathbf{x}_0) = \mathbf{H}_p(\mathbf{x}_0)\mathbf{p}. \tag{4.22}$$

The matrix of weights $\mathbf{H}_p(\mathbf{x}_0)$ can be found using Eq. (3.18) as

$$\begin{aligned} \mathbf{H}_p(\mathbf{x}_0) &= \begin{bmatrix} \mathrm{H}_{pp1}(\mathbf{x}_0) & \mathrm{H}_{pp2}(\mathbf{x}_0) & \mathrm{H}_{pp3}(\mathbf{x}_0) \end{bmatrix} \\ &= \mathbf{L}_p(\mathbf{x}_0)\mathbf{M}^{-1}, \end{aligned} \tag{4.23}$$

where matrices $\mathbf{L}_p(\mathbf{x}_0)$ and $\mathbf{M}$ can be calculated as

$$\mathbf{L}_p(\mathbf{x}_0) = \frac{\left\langle p_i(\mathbf{x}_0)\mathbf{p}_i^{\mathrm{H}}\right\rangle}{\left\langle |p_i|^2\right\rangle} = \left[\begin{array}{ccc} A(\mathbf{x}_0-\mathbf{x}_1) & A(\mathbf{x}_0-\mathbf{x}_2) & A(\mathbf{x}_0-\mathbf{x}_3)\end{array}\right], \quad (4.24)$$

$$\mathbf{M} = \frac{\left\langle \mathbf{p}_i\mathbf{p}_i^{\mathrm{H}}\right\rangle}{\left\langle |p_i|^2\right\rangle} = \left[\begin{array}{ccc} 1 & A(\mathbf{x}_1-\mathbf{x}_2) & A(\mathbf{x}_3-\mathbf{x}_1) \\ A(\mathbf{x}_2-\mathbf{x}_1) & 1 & A(\mathbf{x}_2-\mathbf{x}_3) \\ A(\mathbf{x}_3-\mathbf{x}_1) & A(\mathbf{x}_3-\mathbf{x}_2) & 1\end{array}\right]. \quad (4.25)$$

The best estimate of pressure at the spatially fixed virtual location, $\mathbf{x}_0$, is therefore given by

$$\begin{aligned}\tilde{p}_v(\mathbf{x}_0) &= \mathbf{H}_p(\mathbf{x}_0)\mathbf{p} \\ &= \mathrm{H}_{pp1}(\mathbf{x}_0)p(\mathbf{x}_1) + \mathrm{H}_{pp2}(\mathbf{x}_0)p(\mathbf{x}_2) + \mathrm{H}_{pp3}(\mathbf{x}_0)p(\mathbf{x}_3). \end{aligned} \quad (4.26)$$

It follows that a stochastically optimal estimate of the pressure at the moving virtual location, $\mathbf{x}_v(n)$, using the measured pressures at three points is given by

$$\begin{aligned}\tilde{p}_v(\mathbf{x}_v(n)) &= \mathrm{H}_{pp1}(\mathbf{x}_v(n))p(\mathbf{x}_1) + \mathrm{H}_{pp2}(\mathbf{x}_v(n))p(\mathbf{x}_2) \\ &+ \mathrm{H}_{pp3}(\mathbf{x}_v(n))p(\mathbf{x}_3). \end{aligned} \quad (4.27)$$

Again the accuracy of the pressure estimate at the moving virtual location depends on the distance between the physical and virtual sensors. As this distance increases, the pressure at the virtual location and the measured quantities become uncorrelated and the pressure estimate given by Eq. (4.27) approaches zero.

Following the same method as in Section 3.1.6, an expression for the relative change in mean squared pressure at a point $\mathbf{x}$ in the controlled sound field can be found. In this control strategy, the best estimate of the pressure at a moving virtual location, $\tilde{p_v}(\mathbf{x}_v(n))$, is given by Eq. (4.27). Using Eq. (3.4), the correlation between the total complex pressure at $\mathbf{x}$ and the estimate of the pressure at the moving virtual location is found to be

$$\langle p(\mathbf{x})\tilde{p_v}^{\star}(\mathbf{x}_v(n))\rangle = P_{px}\left\langle |p|^2\right\rangle, \quad (4.28)$$

where

$$\begin{aligned}P_{px} &= (\mathrm{H}_{pp1}(\mathbf{x}_v(n))A(\mathbf{x}-\mathbf{x}_1) + \mathrm{H}_{pp2}(\mathbf{x}_v(n))A(\mathbf{x}-\mathbf{x}_2) \\ &+ \mathrm{H}_{pp3}(\mathbf{x}_v(n))A(\mathbf{x}-\mathbf{x}_3))\left\langle |p|^2\right\rangle. \end{aligned} \quad (4.29)$$

Using Eqs. (3.4) and (3.8), it can be shown that the mean squared pressure estimate at the moving virtual location, using Eq. (4.27), is related to the total mean squared pressure by

$$\left\langle |\tilde{p}(\mathbf{x}_v(n))|^2 \right\rangle = P_0(n) \left\langle |p|^2 \right\rangle, \tag{4.30}$$

where

$$\begin{aligned} P_0 &= \left(\mathrm{H}^2{}_{pp1}(\mathbf{x}_v(n)) + \mathrm{H}^2{}_{pp2}(\mathbf{x}_v(n)) + \mathrm{H}^2{}_{pp3}(\mathbf{x}_v(n)) \right. \\ &+ 2\mathrm{H}_{pp1}(\mathbf{x}_v(n))\mathrm{H}_{pp2}(\mathbf{x}_v(n))A(\mathbf{x}_1 - \mathbf{x}_2) \\ &+ 2\mathrm{H}_{pp2}(\mathbf{x}_v(n))\mathrm{H}_{pp3}(\mathbf{x}_v(n))A(\mathbf{x}_2 - \mathbf{x}_3) \\ &+ \left. 2\mathrm{H}_{pp1}(\mathbf{x}_v(n))\mathrm{H}_{pp3}(\mathbf{x}_v(n))A(\mathbf{x}_1 - \mathbf{x}_3) \right) \left\langle |p|^2 \right\rangle. \end{aligned} \tag{4.31}$$

By substituting Eqs. (4.28) and (4.30) into Eq. (3.71), the weight function $h_{pp}(\mathbf{x})$ is found to be

$$h_{pp}(\mathbf{x}) = \frac{P_{px}}{P_0}. \tag{4.32}$$

As stated in Section 3.1.6, the space-average mean squared pressure at $\mathbf{x}$, which is uncorrelated with $\tilde{p}(\mathbf{x}_v(n))$, is

$$\left\langle |p_{uu}(\mathbf{x})|^2 \right\rangle = \left\langle |p|^2 \right\rangle - |h_{pp}(\mathbf{x})|^2 \left\langle |\tilde{p}(\mathbf{x}_v(n))|^2 \right\rangle. \tag{4.33}$$

By substituting Eqs. (4.30) and (4.32) into Eq. (4.33), the space-average uncorrelated pressure becomes

$$\left\langle |p_{uu}(\mathbf{x})|^2 \right\rangle = \left(1 - \frac{P_{px}^2}{P_0} \right) \left\langle |p|^2 \right\rangle. \tag{4.34}$$

When $\tilde{p}(\mathbf{x}_v(n))$ is cancelled with a single control source the residual pressure at $\mathbf{x}$ is, according to Eq. (3.69), $p_{uu}(\mathbf{x})$ only. Therefore, the mean squared pressure at a position $\mathbf{x}$ in the controlled sound field is given by

$$\left\langle |p(\mathbf{x})|^2 \right\rangle = \left(1 - \frac{P_{px}^2}{P_0} \right) \left\langle |p|^2 \right\rangle. \tag{4.35}$$

When the pressure at the moving virtual location, estimated using the pressures at the three points, is cancelled with a single secondary source, the relative change in

mean squared pressure is given by

$$\frac{\left\langle |p(\mathbf{x})|^2 \right\rangle}{\left\langle |p_p|^2 \right\rangle} = \left(1 - \frac{P_{px}^2}{P_0}\right) \alpha. \tag{4.36}$$

4.2 Experimental method

The performance of an active noise control system in generating a zone of quiet at a moving virtual microphone located at the ear of a rotating artificial head was investigated in real-time experiments. In the experiments, each of the moving virtual sensing methods were used to generate a single moving virtual microphone at one of the ears of the rotating artificial head. The experimental results illustrate the level of attenuation that can be expected at an ear of a seated observer in practice.

Experiments were conducted in a three-dimensional cavity with dimensions of 1000 mm × 800 mm × 890 mm, as shown in Fig. 4.3. A HEAD acoustics HMS III.0 Artificial Head mounted on a turntable to simulate head rotation was located in the centre of the cavity, as shown in Fig. 4.4. The artificial head has overall dimensions of 465 mm × 400 mm × 180 mm to approximate the size of a human head. The turntable was position controlled to generate 90° head rotations from −45° to +45° which is typical of the full head rotations capable of a seated observer. The desired trajectory of the artificial head and of the virtual microphone was a triangular waveform with peak amplitudes of ±45°. The expression for the triangular waveform governing the desired head rotations, in degrees, is given by

$$\theta_h(n) = \frac{180}{\pi} arcsin\left(sin\left(\frac{2\pi n}{t_v f_s}\right)\right), \tag{4.37}$$

where n is the time sample, t_v is the period of head motion and $f_s = 3.5$ kHz the sampling frequency. An electret microphone was located at an ear of the artificial head to measure the performance at the virtual microphone position.

4.2.1 Physical sensor configurations

The arrangement of the physical sensors around the artificial head is different for each of the moving virtual sensing algorithms presented in this chapter. The remote moving microphone technique uses the error signal from a single physical microphone to obtain an estimate of the error signal at the moving virtual location. The arrangement of the artificial head and the physical and virtual microphones for the

Figure 4.3: The three-dimensional cavity used in real-time experiments. The fixed frame supports the physical microphones.

Figure 4.4: The HEAD acoustics HMS III.0 Artificial Head mounted on a turntable and located in the centre of the cavity.

remote moving microphone technique is shown in Fig. 4.5. As shown in Fig. 4.5, the physical microphone is located 4 cm from the virtual microphone when the artificial head is positioned at $\theta_h = 0°$.

The adaptive LMS moving virtual microphone technique estimates the error signal at the moving virtual location as the sum of the weighted physical sensor signals at M_a physical microphones in an array. In experiments, four different configurations of physical microphones were investigated to determine which configuration results in the most accurate estimate of the moving virtual error signal. Firstly, $M_a = 3$ physical microphones were arranged in linear formation perpendicular to the head surface, as shown in Fig. 4.6. In this formation, the physical microphone closest to the headform is located 3 cm from the ear when the artificial head is positioned at $\theta_h = 0°$ and the physical microphone spacing is 2 cm. The $M_a = 3$ physical microphones were arranged in linear formation parallel to the head surface, as shown in Fig. 4.7. When in linear parallel formation, the centre microphone is located 4 cm from the ear when the artificial head is positioned at $\theta_h = 0°$ and the physical microphone spacing is 2 cm. The $M_a = 3$ physical microphones were also arranged in triangular formation around the artificial head, as shown in Fig. 4.8. In this case, the three physical microphones are located on the corners of an isosceles triangle with equal angles of 30°. The final physical sensor arrangement consisted of $M_a = 4$ physical microphones in a tetrahedral formation. In this configuration, the four physical microphones are positioned on the corners of a regular tetrahedron with an edge length of 8 cm, as shown in Fig. 4.9. The tetrahedral configuration of physical microphones is positioned near the artificial head such that the centroid of the tetrahedron is located in the plane of the ear.

The SOTDF moving virtual sensing method is implemented in three forms; using the measured pressure and pressure and gradient at a point, the measured pressures at two points or the measured pressures at three points. Using the measured pressure and pressure gradient to estimate the moving virtual error signal requires simultaneous measurement of the pressure and pressure gradient at the same point and this was done using the two microphone technique (Fahy, 1995) in real-time experiments. In the two-microphone technique, the pressure is estimated midway between two physical microphones and the pressure gradient is calculated using a finite difference approximation. When using the measured pressure and pressure gradient at a point or the pressures at two points to estimate the moving virtual error signal, the two physical microphones were arranged in linear parallel formation, as shown in Fig. 4.7. In this case, the centre point between the two physical microphones is

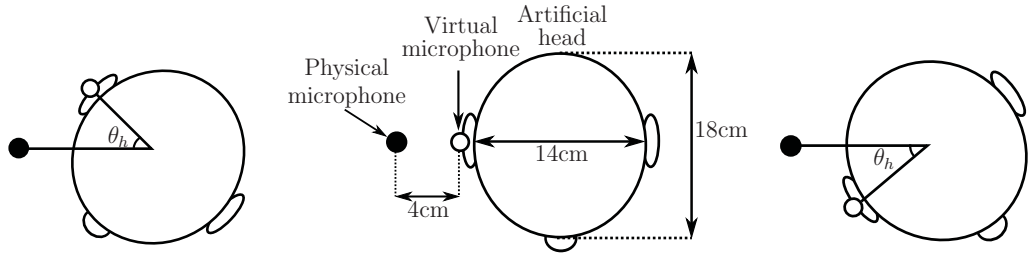

(a) $\theta_h = -45°$. (b) $\theta_h = 0°$. (c) $\theta_h = 45°$.

Figure 4.5: The physical arrangement of the artificial head and the physical and virtual microphones for the remote moving microphone technique for a three-dimensional sound field. The physical microphone is indicated by a solid circle marker and the virtual microphone is indicated by an open circle marker.

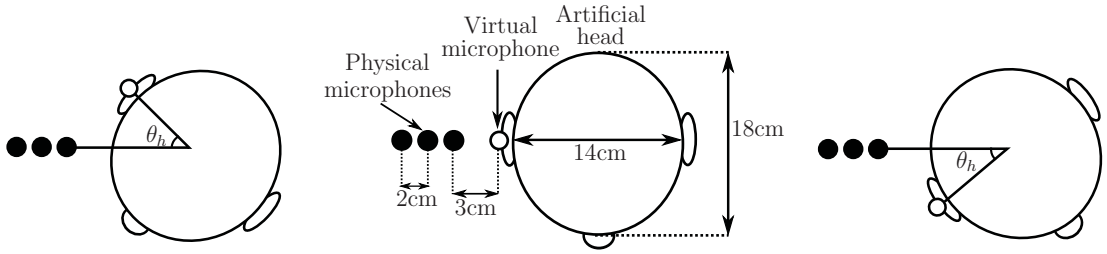

(a) $\theta_h = -45°$. (b) $\theta_h = 0°$. (c) $\theta_h = 45°$.

Figure 4.6: The physical arrangement of the artificial head and the physical and virtual microphones for the adaptive LMS moving virtual microphone technique for a three-dimensional sound field when the physical microphones are arranged in linear perpendicular formation. The physical microphones are indicated by solid circle markers and the virtual microphone is indicated by an open circle marker.

4 cm from the ear when the artificial head is positioned at $\theta_h = 0°$ and the physical microphone spacing is 2 cm. When using the measured pressures at three points to estimate the moving virtual error signal, the three physical microphones were arranged in triangular formation as is shown in Fig. 4.8.

A summary of physical sensor configurations used in each of the moving virtual sensing methods is given in Table 4.1. In real-time experiments, the physical microphones were positioned around the headform using a fixed frame which can be seen in Fig. 4.3. The physical microphones and the additional microphone measuring the performance at the ear of the artificial head were connected to a combined power supply and amplifier. The amplified error signals were then sent through a 16-bit PCI-DAS1602/16 multifunction analog & digital I/O Board from Measurement

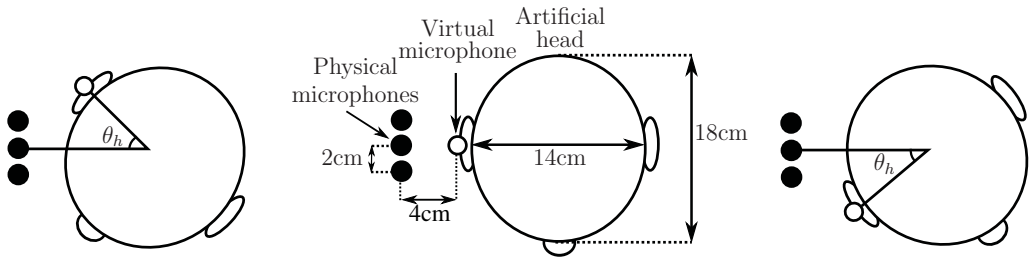

(a) $\theta_h = -45°$. (b) $\theta_h = 0°$. (c) $\theta_h = 45°$.

Figure 4.7: The physical arrangement of the artificial head and the physical and virtual microphones for the adaptive LMS moving virtual microphone technique for a three-dimensional sound field when the physical microphones are arranged in linear parallel formation. The physical microphones are indicated by solid circle markers and the virtual microphone is indicated by an open circle marker.

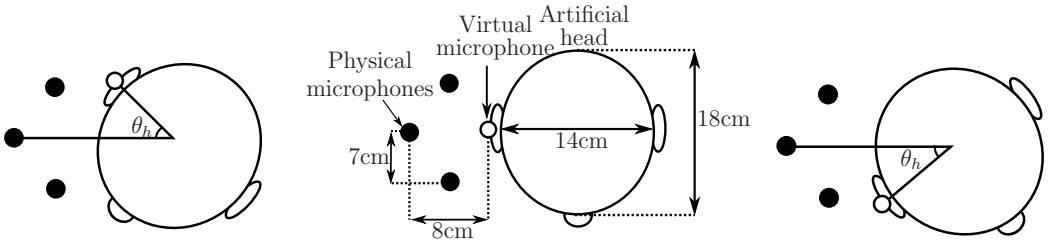

(a) $\theta_h = -45°$. (b) $\theta_h = 0°$. (c) $\theta_h = 45°$.

Figure 4.8: The physical arrangement of the artificial head and the physical and virtual microphones for the adaptive LMS moving virtual microphone technique for a three-dimensional sound field when the physical microphones are arranged in triangular formation. The physical microphones are indicated by solid circle markers and the virtual microphone is indicated by an open circle marker.

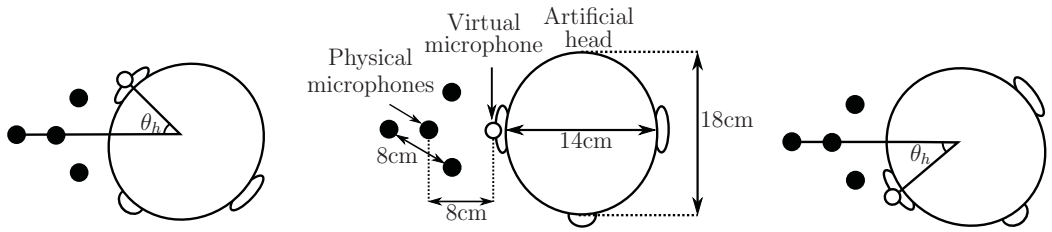

(a) $\theta_h = -45°$. (b) $\theta_h = 0°$. (c) $\theta_h = 45°$.

Figure 4.9: The physical arrangement of the artificial head and the physical and virtual microphones for the adaptive LMS moving virtual microphone technique for a three-dimensional sound field when the physical microphones are arranged in tetrahedral formation. The physical microphones are indicated by solid circle markers and the virtual microphone is indicated by an open circle marker.

Computing, which was used as a 16-channel AD-converter.

4.2.2 Actuator configuration

Two 4" loudspeakers were located in the opposite corners of the three-dimensional cavity, one to generate the tonal primary sound field and the other to act as the secondary source. The loudspeakers were each excited by control signals which were first passed through a 16-bit PCI-DDA08/16 analog output board from Measurement Computing. This output board was used as an 8-channel DA-converter and an amplifier.

The performance of the moving virtual sensing algorithms was investigated at the primary excitation frequency of 525 Hz. An excitation frequency of 525 Hz corresponds to the 33rd acoustic resonance of the three-dimensional cavity. At this frequency the modal overlap is $M \simeq 4$, illustrating that the sound field is modally dense, as a modal overlap of $M = 3$ defines the boundary between low and high modal density (Nelson and Elliott, 1992). The performance of the moving virtual sensing algorithms was also investigated off resonance, at an excitation frequency of 510 Hz. An excitation frequency of 510 Hz lies between the 31st and 32nd resonant frequency of the cavity. For both excitation frequencies of 525 Hz and 510 Hz, the performance at the moving virtual location was measured for two different periods of 90° head rotation; $t_v = 5$ s and $t_v = 10$ s.

The control signal to the secondary loudspeaker, $u_s(n)$, was generated using a modified version of the filtered-x LMS algorithm for moving virtual sensing which is discussed in the following section.

Table 4.1: Summary of the physical sensor configurations used in the moving virtual sensing experiments.

Algorithm	Physical sensor configurations
The remote moving microphone technique	• Single microphone
The adaptive LMS moving virtual microphone technique	• 2 microphones in linear perpendicular formation • 3 microphones in linear parallel formation • 3 microphones in icoseles triangular formation • 4 microphones in regular tetrahedral formation
The SOTDF moving virtual sensing method	• Using the measured pressure and pressure gradient at a point - 2 microphones in linear parallel formation (two-microphone technique) • Using the measured pressures at 2 points - 2 microphones in linear parallel formation • Using the measured pressures at 3 points - 3 microphones in triangular formation

4.2.3 The filtered-x LMS algorithm for moving virtual sensing

The most commonly implemented adaptive algorithm in feedforward active noise control systems is the filtered-x LMS algorithm (Kuo and Morgan, 1996, Elliott, 2001). The filtered-x LMS algorithm generates the control signal, $u_s(n)$, that drives the secondary sound source during real-time control. This algorithm, while being relatively simple to implement, is robust and in most cases quick to converge to a near-optimal solution (Kuo and Morgan, 1996, Elliott, 2001).

The filtered-x LMS algorithm is based upon the method of steepest descent which has the form

$$\mathbf{w}(n+1) = \mathbf{w}(n) - \mu\Delta\mathbf{w}(n), \tag{4.38}$$

where $\mathbf{w}(n)$ is a vector of H filter coefficients, $\Delta\mathbf{w}(n)$ is the gradient of the error criterion with respect to the filter weights and μ is the convergence coefficient. The error criterion is selected to be a positive definite function of the filter coefficients (Sommerfeldt and Nashif, 1994). As this error criterion is quadratic with respect to the filter coefficients it can be represented as a hyperparabolic surface in $H+1$ dimensional space. The steepest descent algorithm given in Eq. (4.38) incrementally moves the weights along the error surface following the negative gradient of the error criterion until the weights reach the optimal solution.

The filtered-x LMS algorithm is used to generate the control signal, $u_s(n)$, that drives the secondary source to minimise the estimated moving virtual error signal, $\tilde{p}_v(n)$, at the ear of the rotating artificial head. This adaptive algorithm requires a reference signal, $x(n)$, that is highly correlated with the primary disturbance and uses the moving virtual error signal, $\tilde{p}_v(n)$, as feedback.

The filtered-x LMS algorithm is given by

$$\mathbf{w}(n+1) = \mathbf{w}(n) - \mu\tilde{\mathbf{r}}_v(n)\tilde{p}_v(n), \tag{4.39}$$

where $\mathbf{w}(n)$ is the vector of the H controller filter coefficients given by

$$\mathbf{w}(n) = \left[\begin{array}{cccc} w_0(n) & w_1(n) & \ldots & w_{H-1}(n) \end{array} \right]^{\mathrm{T}}, \tag{4.40}$$

μ is the convergence coefficient and $\tilde{\mathbf{r}}_v(n)$ is a vector of H filtered reference signals given by

$$\tilde{\mathbf{r}}_v(n) = \left[\begin{array}{cccc} \tilde{r}_v(n) & \tilde{r}_v(n-1) & \ldots & \tilde{r}_v(n-H+1) \end{array} \right]^{\mathrm{T}}, \tag{4.41}$$

where $\tilde{r}_v(n)$ is the virtual filtered reference signal at the moving virtual location. The virtual filtered reference signal, $\tilde{r}_v(n)$, is obtained by filtering a reference signal which is strongly correlated with the primary disturbance, $x(n)$, by the virtual secondary transfer matrix $\tilde{\mathbf{Z}}_{sv}$ measured at the $\bar{M}_v$ spatially fixed virtual locations, $\bar{\mathbf{x}}_v$. This results in a vector, $\tilde{\mathbf{r}}_{\bar{v}}(n)$, of the $\bar{M}_v$ virtual filtered reference signals at the spatially fixed virtual locations $\bar{\mathbf{x}}_v$

$$\tilde{\mathbf{r}}_{\bar{v}}(n) = \left[\begin{array}{cccc} \tilde{r}_{v1}(n) & \tilde{r}_{v2}(n) & \ldots & \tilde{r}_{v\bar{M}_v}(n) \end{array} \right]^{\mathrm{T}}. \tag{4.42}$$

An estimate of the virtual filtered reference signal, $\tilde{r}_v(n)$, at the moving virtual location is obtained by interpolating the virtual filtered reference signals in $\tilde{\mathbf{r}}_{\bar{v}}(n)$ over three-dimensions.

The control signal to the secondary sound source is now calculated as

$$u_s(n) = \mathbf{x}^{\mathrm{T}}(n)\mathbf{w}(n), \tag{4.43}$$

where the vector of reference signals $\mathbf{x}(n)$ is defined as

$$\mathbf{x}(n) = \left[\begin{array}{cccc} x(n) & x(n-1) & \ldots & x(n-H+1) \end{array} \right]^{\mathrm{T}}. \tag{4.44}$$

In the experiments, the secondary transfer function matrix at the spatially fixed virtual locations, $\tilde{\mathbf{Z}}_{sv}$, was modelled as a matrix of FIR filters defined as

$$\tilde{\mathbf{Z}}_{sv} = \left[\begin{array}{cccc} \tilde{Z}_{\mathrm{sv},1} & \tilde{Z}_{\mathrm{sv},2} & \ldots & \tilde{Z}_{sv,\bar{M}_v} \end{array} \right]^{\mathrm{T}}, \tag{4.45}$$

where each $\tilde{Z}_{sv,\bar{M}_v}$ is an FIR filter that models the impulse response between the secondary source and the $\bar{M}_v$th spatially fixed virtual location. The gradient descent algorithm, as stated in Eq. (4.38), can be used to adjust the filter weights so that the impulse response of the FIR filters matches the secondary transfer functions. For broadband primary disturbances, a pseudo-random noise signal is used. However, as the primary disturbance in these experiments was tonal, the secondary transfer functions only need to be accurate at the disturbance frequency and were implemented using a two coefficient FIR filter (Hansen, 2001).

4.2.4 Real-time implementation

The moving virtual sensing algorithms and the modified filtered-x LMS algorithm (discussed in Section (4.2.3)) were implemented in real-time using a host-target software program named xPC Target (Mathworks, 2007a,b). For real-time implementation, xPC Target requires a host PC and a separate target PC. In this case, the host PC was a laptop with Matlab and Simulink installed to create a model of the active noise control system. To run the real-time experiments, the I/O blocks in the Simulink model were connected to the microphones and loudspeakers. Using Real-Time Workshop and a C compiler, executable code was then created from the Simulink model on the host PC. This executable code was then downloaded from the host PC to the target PC, running the xPC Target real-time kernel, via a TCP/IP network connection. The target application was then run in real-time with the real-time data viewed and stored on the host PC (Mathworks, 2007a,b).

Before implementing active noise control, the remote moving microphone technique and the modified filtered-x LMS algorithm both require a preliminary identification stage in which the necessary primary and secondary transfer functions are measured at a number, $\bar{M}_v$, of spatially fixed virtual locations, $\bar{\mathbf{x}}_v$. In the preliminary identification stage, the microphone at the ear of the rotating artificial head was placed at $\bar{M}_v = 31$ spatially fixed virtual locations, $\bar{\mathbf{x}}_v$, equally spaced along the 90° arc of head rotation. The required primary and secondary transfer functions were modelled as two coefficient FIR filters during this preliminary identification stage because the primary disturbance was tonal.

The adaptive LMS moving virtual microphone technique also requires a preliminary identification stage in which the physical secondary transfer functions are measured and the matrices of the primary and secondary weights, $\mathbf{w}_p$ and $\mathbf{w}_s$, are estimated at the $\bar{M}_v$ spatially fixed virtual locations, $\bar{\mathbf{x}}_v$. In experiments, these secondary transfer functions and the matrices of weights were estimated at the $\bar{M}_v = 31$ spatially fixed virtual locations, $\bar{\mathbf{x}}_v$, equally spaced along the 90° arc of head rotation during the preliminary identification stage.

4.3 Results

The experimental results of active noise control at a moving virtual microphone located at the ear of the rotating artificial head are given in this section. In the real-time experiments, each of the moving virtual sensing algorithms was used to estimate

the error signal at the virtual microphone that tracks the ear of the rotating artificial head. This estimate of the pressure at the virtual location was then minimised with the active noise control system to generate a zone of quiet at the ear of the rotating artificial head. Experimental results obtained with the remote moving microphone technique, the adaptive LMS moving virtual microphone technique, and the SOTDF moving virtual sensing method are presented as follows.

It should be noted that for brevity, only the main experimental findings are described in the following sections. More detailed descriptions of the figures can be found in Appendix B.

4.3.1 The remote moving microphone technique for a three-dimensional sound field

Figs. 4.10 and 4.11 show the attenuation achieved at the moving virtual location with the remote moving microphone technique at the 525 Hz resonance and off resonance at 510 Hz respectively. Control profiles are shown for active noise control at the moving virtual microphone, a fixed virtual microphone located at the ear of the artificial head when $\theta_h = 0°$, and the fixed physical microphone. The control performance at the ear of the artificial head is shown for the period of head rotation being $t_v = 10$ s in part (a) of Figs. 4.10 and 4.11 and $t_v = 5$ s in part (b) of Figs. 4.10 and 4.11. Part (c) of Figs. 4.10 and 4.11 shows the desired trajectory of the artificial head and of the moving virtual microphone, in degrees, compared to the actual controlled head position. The transient behaviour seen in Figs. 4.10 and 4.11 at time $t/t_v = 0$ s, for both $t_v = 5$ s and $t_v = 10$ s, is caused by the controller initialising. A detailed description of each of these figures is given in Appendix B.1.

Table 4.2 gives the time average and standard deviation of the attenuation achieved at the moving virtual location with the remote moving microphone technique. Tabulated results are given for active noise control at the moving virtual microphone, a fixed virtual microphone located at the ear of the artificial head when $\theta_h = 0°$, and the physical microphone, for the two excitation frequencies of 525 Hz and 510 Hz and for the period of head rotation being $t_v = 10$ s and $t_v = 5$ s.

For both periods of head rotation and for both excitation frequencies, the control profiles in Figs. 4.10 and 4.11 show that minimising the moving virtual error signal achieves the best control performance at the ear of the rotating artificial head. Table 4.2 reveals that both on and off resonance, active noise control at the moving virtual microphone provides up to an additional 10.8 dB of attenuation at the moving virtual

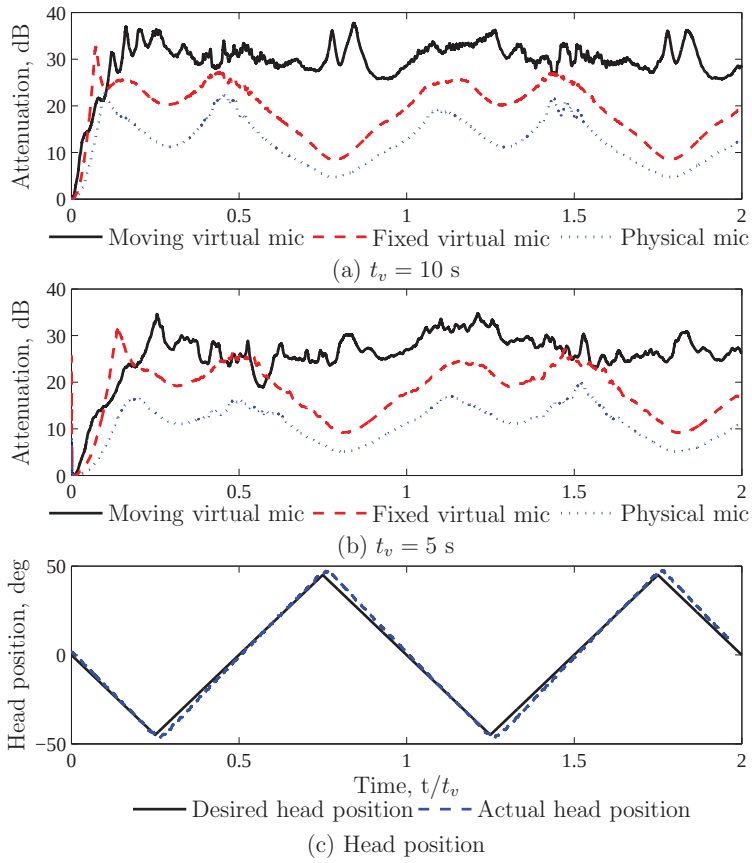

Figure 4.10: Tonal attenuation achieved at the 525 Hz resonance with the remote moving microphone technique for a three-dimensional sound field. Control profiles are shown for active noise control at the moving virtual microphone, a virtual microphone spatially fixed at $\theta = 0°$, and the physical microphone, for a period of rotation (a) $t_v = 10$ s; (b) $t_v = 5$ s; and (c) head position.

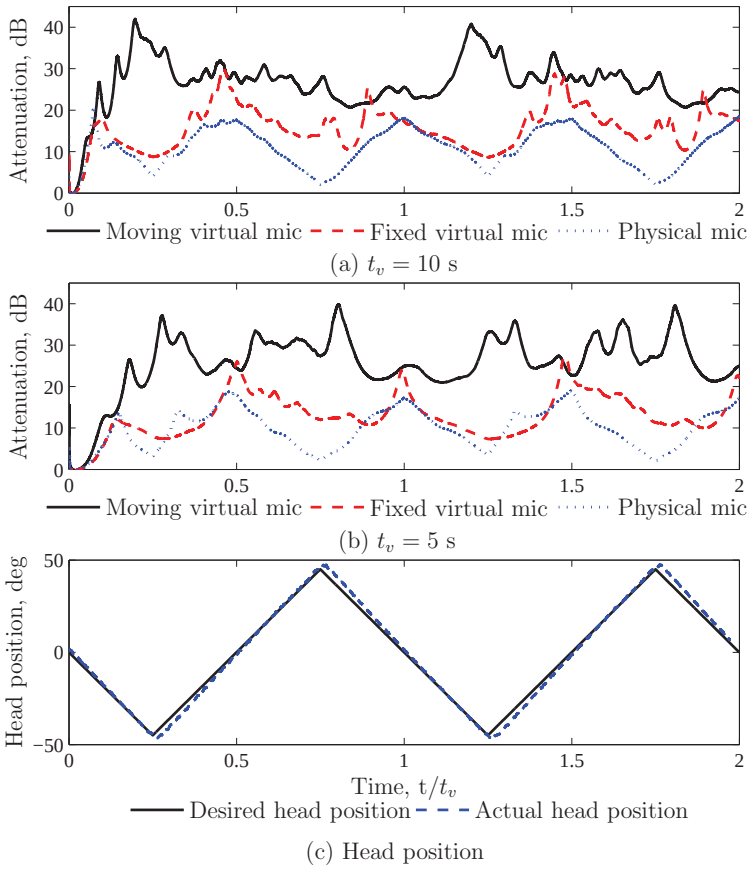

Figure 4.11: Tonal attenuation achieved off resonance at 510 Hz with the remote moving microphone technique for a three-dimensional sound field. Control profiles are shown for active noise control at the moving virtual microphone, a virtual microphone spatially fixed at $\theta = 0°$, and the physical microphone, for a period of rotation (a) $t_v = 10$ s; (b) $t_v = 5$ s; and (c) head position.

Table 4.2: Time average and standard deviation (shown in parentheses) of the attenuation in dB achieved at the moving virtual location with the remote moving microphone technique for a three-dimensional sound field. Results achieved in a modified sound field (discussed in Section 4.3.1.1) are highlighted in grey. Tabulated results are given for active noise control at the moving virtual microphone, a fixed virtual microphone located at the ear of the artificial head when $\theta_h = 0°$, and the physical microphone.

t_v s	525 Hz			510 Hz		
	Moving virtual mic	Fixed virtual mic	Physical mic	Moving virtual mic	Fixed virtual mic	Physical mic
10	29.7(4.7)	18.9(6.1)	12.3(5.6)	26.5(5.1)	15.7(5.2)	10.8(4.6)
5	25.9(5.3)	18.1(6.2)	10.9(4.9)	24.6(5.6)	13.9(5.3)	9.7(4.7)
10	18.1(5.3)	14.7(5.5)	10.4(5.4)	16.9(5.3)	12.1(5.5)	9.6(5.4)
5	17.3(5.6)	13.9(5.7)	8.6(5.3)	16.7(6.1)	11.7(6.5)	8.4(5.2)

location compared to active noise control at the fixed virtual microphone. Instead of minimising the fixed physical error signal, minimising the moving virtual error signal generates up to an additional 17.4 dB of attenuation at resonance and up to an additional 15.7 dB of attenuation off resonance.

Comparing Figs. 4.10 and 4.11 demonstrates that reduced control performance is achieved off resonance when either the moving virtual error signal, the fixed virtual error signal or the physical error signal are minimised. This is to be expected since several modes now dominate the cavity response. A decrease in the attenuation achieved off resonance can be seen in Table 4.2 by comparing the time average attenuations achieved at the moving virtual location for the two excitation frequencies.

Comparing parts (a) and (b) of Figs. 4.10 and 4.11 shows that when the period of head rotation is reduced, the control performance reduces. Table 4.2 also shows a decrease in the average attenuation achieved at the moving virtual location and an increase in the standard deviation with a decrease in the period of head rotation. Such a result is to be expected because it takes a finite time for the controlled sound field to stabilise, so once the period of head rotation nears the reverberation time of the cavity, the control performance is compromised.

4.3.1.1 Robustness of the remote moving microphone technique for a three-dimensional sound field

The remote moving microphone technique computes an estimate of the pressure at the moving virtual location by interpolating the virtual error signals at a number of spatially fixed virtual locations estimated using the remote microphone technique (Roure and Albarrazin, 1999). To estimate the virtual error signals at the spatially fixed virtual locations, the remote microphone technique requires a preliminary identification stage and models of the required primary and secondary transfer functions. The remote moving microphone technique is therefore not robust to changes in the sound field that may alter the transfer functions between the error sensors and the sources. To investigate the robustness of this moving virtual sensing method, the performance of the active noise control system in generating a zone of quiet at the moving virtual microphone was examined after modifying the sound field. Firstly, the preliminary identification stage was conducted in which the required transfer functions were measured for the rotating artificial head and the physical sensors located at a certain position within the cavity. Once the preliminary identification stage was complete, the rotating artificial head and the physical sensors were moved 3 cm ($\approx 5\%$ of λ) within the cavity to a new position while ensuring the relative arrangement of the physical and virtual sensors remained constant. Changing the position of the experimental equipment within the cavity is equivalent to a significant shift in the sound field. The performance of the active noise control system in generating a zone of quiet at the ear of the rotating artificial head was then investigated at this new position using the transfer functions measured at the original position in the preliminary identification stage.

It should be noted that this is not a definitive robustness study (like a Monte Carlo simulation) but rather one example of the performance of the remote moving microphone technique in a perturbed sound field. This study, investigating the affect of a modified sound field on moving virtual sensing, illustrates the problems this moving virtual sensing technique faces in practice.

Figs. 4.12 and 4.13 show the performance of the active noise control system in generating a zone of quiet at the virtual microphone with the remote moving microphone technique after modifying the sound field. The attenuation achieved at the moving virtual location is shown at the 525 Hz resonance and off resonance at 510 Hz in Figs. 4.12 and 4.13 respectively. Control profiles are shown for active noise control at the moving virtual microphone, a fixed virtual microphone located

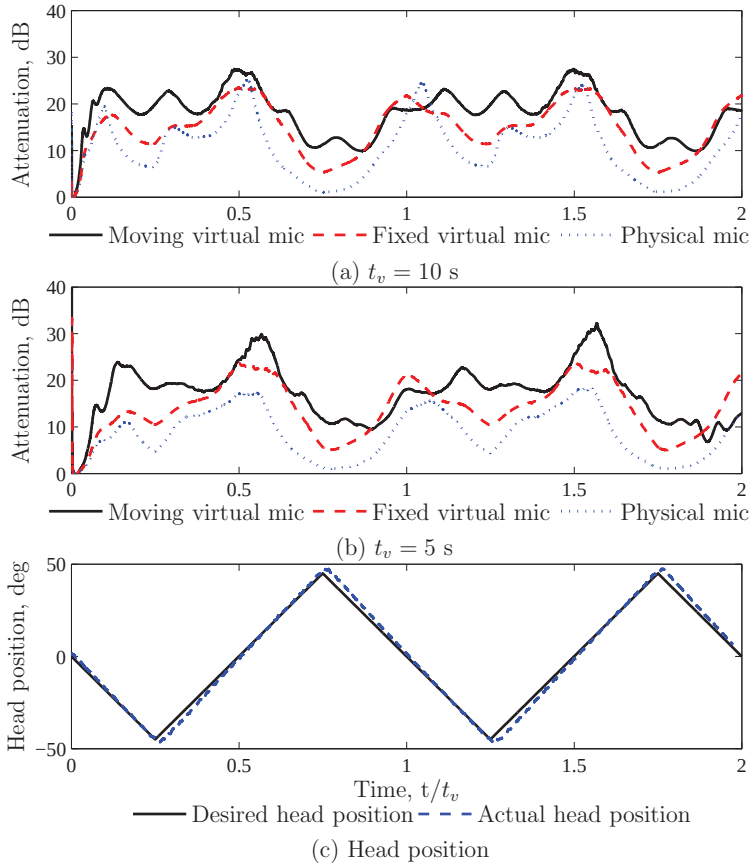

Figure 4.12: Tonal attenuation achieved at the 525 Hz resonance with the remote moving microphone technique for a three-dimensional sound field after modifying the sound field. Control profiles are shown for active noise control at the moving virtual microphone, a virtual microphone spatially fixed at $\theta = 0°$, and the physical microphone, for a period of rotation (a) $t_v = 10$ s; (b) $t_v = 5$ s; and (c) head position.

at the ear of the artificial head when $\theta_h = 0°$, and the fixed physical microphone. The control performance at the ear of the artificial head is shown for the period of head rotation being $t_v = 10$ s in part (a) of Figs. 4.12 and 4.13 and $t_v = 5$ s in part (b) of Figs. 4.12 and 4.13. Part (c) of Figs. 4.12 and 4.13 shows the desired trajectory of the artificial head and of the moving virtual microphone, in degrees, compared to the actual controlled head position. A detailed description of each of these figures is given in Appendix B.1.1.

The time average and standard deviation of the attenuation achieved with the remote moving microphone technique after modification of the sound field is given in the grey shaded section of Table 4.2. Tabulated results are given for active noise control at the moving virtual microphone, a fixed virtual microphone located at the

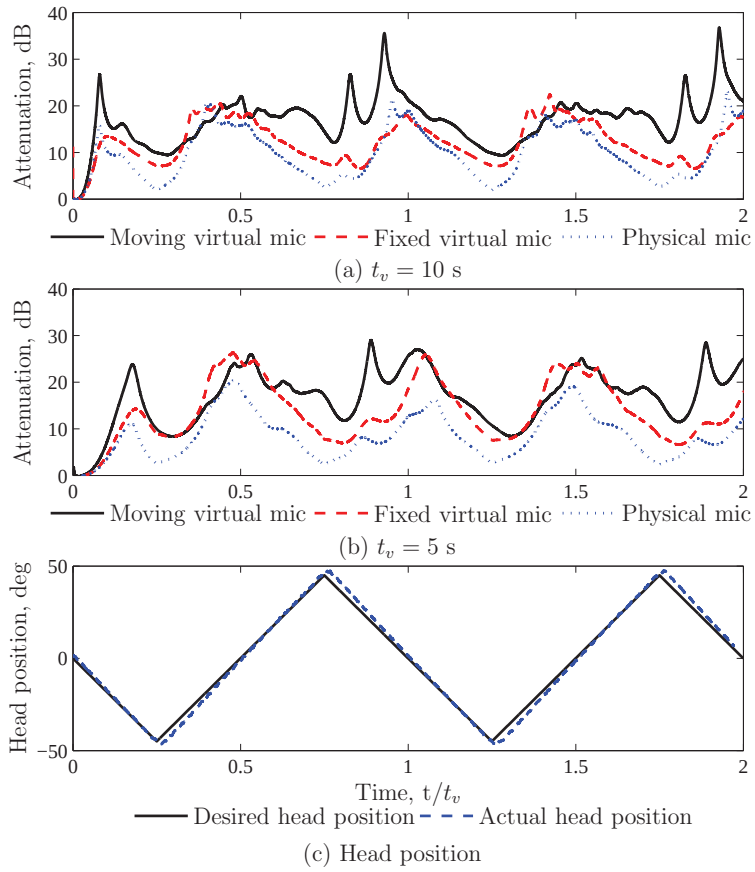

Figure 4.13: Tonal attenuation achieved off resonance at 510 Hz with the remote moving microphone technique for a three-dimensional sound field after modifying the sound field. Control profiles are shown for active noise control at the moving virtual microphone, a virtual microphone spatially fixed at $\theta = 0°$, and the physical microphone, for a period of rotation (a) $t_v = 10$ s; (b) $t_v = 5$ s; and (c) head position.

ear of the artificial head when $\theta_h = 0°$, and the physical microphone, for the two excitation frequencies of 525 Hz and 510 Hz and for the period of head rotation being $t_v = 10$ s and $t_v = 5$ s.

The control profiles in Figs. 4.12 and 4.13 demonstrate that minimising the moving virtual error signal achieves the best control performance at the moving virtual location even after modification of the sound field. Table 4.2 reveals that active noise control at the moving virtual microphone after modifying the sound field provides up to an additional 5.0 dB of attenuation at the moving virtual location compared to active noise control at the fixed virtual microphone. After modifying the sound field, minimising the moving virtual error signal achieves up to an additional 8.7 dB of attenuation at the moving virtual location compared to minimising the fixed physical error signal. There is however, a significant reduction in control performance when active noise control is performed in a modified sound field compared to in an unmodified sound field. Table 4.2 shows that the attenuation achieved by minimising the moving virtual error signal is reduced by up to 11.6 dB when active noise control is performed in the modified the sound field. Minimising the fixed virtual error signal after modifying the sound field reduces the attenuation achieved at the moving virtual location by up to 4.2 dB. This indicates a lack of robustness in the remote moving microphone technique and that this moving virtual sensing method is adversely affected by changes in the sound field that alter the transfer functions between the error sensors and the sources.

4.3.2 The adaptive LMS moving virtual microphone technique for a three-dimensional sound field

The attenuation achieved at the moving virtual location with the adaptive LMS moving virtual microphone technique at the 525 Hz resonance is shown in Figs. 4.14 - 4.17. These figures show the control performance achieved when $M_a = 3$ physical microphones are in linear formation perpendicular to the head, $M_a = 3$ physical microphones are in linear formation parallel to the head, $M_a = 3$ physical microphones are in triangular formation, and $M_a = 4$ physical microphones are in tetrahedral formation respectively. Control profiles are shown for active noise control at the moving virtual microphone, a fixed virtual microphone located at the ear of the artificial head when $\theta_h = 0°$, and a fixed physical microphone located 4 cm from the ear when $\theta_h = 0°$. The control performance at the ear of the artificial head is shown for the period of head rotation being $t_v = 10$ s in part (a) of Figs. 4.14 - 4.17

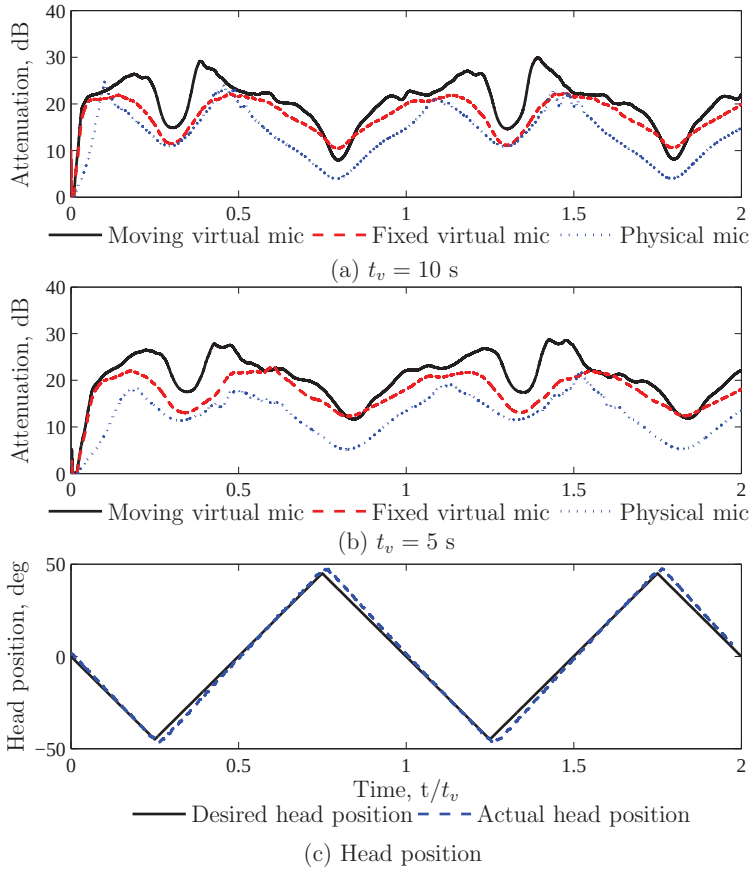

(a) $t_v = 10$ s

(b) $t_v = 5$ s

(c) Head position

Figure 4.14: Tonal attenuation achieved at the 525 Hz resonance with the adaptive LMS moving virtual microphone technique for a three-dimensional sound field when $M_a = 3$ physical microphones are in linear perpendicular configuration. Control profiles are shown for active noise control at the moving virtual microphone, a virtual microphone spatially fixed at $\theta = 0°$, and the physical microphone, for a period of rotation (a) $t_v = 10$ s; (b) $t_v = 5$ s; and (c) head position.

and $t_v = 5$ s in part (b) of Figs. 4.14 - 4.17. Part (c) of Figs. 4.14 - 4.17 shows the desired trajectory of the artificial head and of the moving virtual microphone, in degrees, compared to the actual controlled head position. As previously stated, the transient behaviour seen in Figs. 4.14 - 4.17 at time $t/t_v = 0$ s for both $t_v = 5$ s and $t_v = 10$ s, is caused by the controller initialising. A detailed description of each of these figures is given in Appendix B.2.

The control profiles in Figs. 4.14 - 4.17 all show that minimising the moving virtual error signal achieves the best control performance at the ear of the rotating artificial head regardless of the number or arrangement of the physical microphones. By comparing Figs. 4.14 - 4.17 it is clear that arranging $M_a = 4$ physical microphones

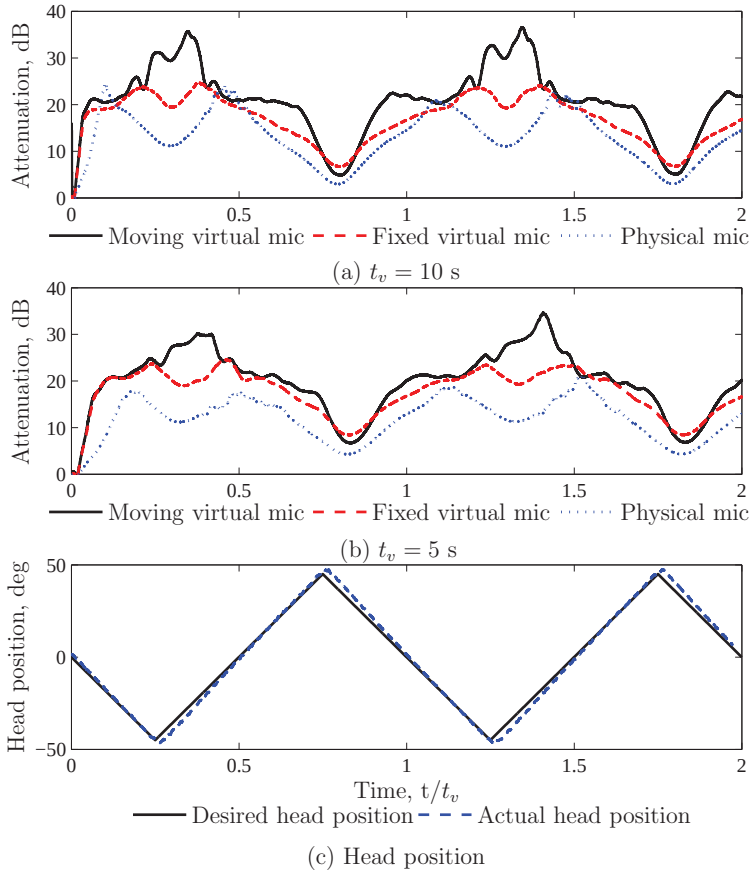

(a) $t_v = 10$ s

(b) $t_v = 5$ s

(c) Head position

Figure 4.15: Tonal attenuation achieved at the 525 Hz resonance with the adaptive LMS moving virtual microphone technique for a three-dimensional sound field when $M_a = 3$ physical microphones are in linear parallel configuration. Control profiles are shown for active noise control at the moving virtual microphone, a virtual microphone spatially fixed at $\theta = 0°$, and the physical microphone, for a period of rotation (a) $t_v = 10$ s; (b) $t_v = 5$ s; and (c) head position.

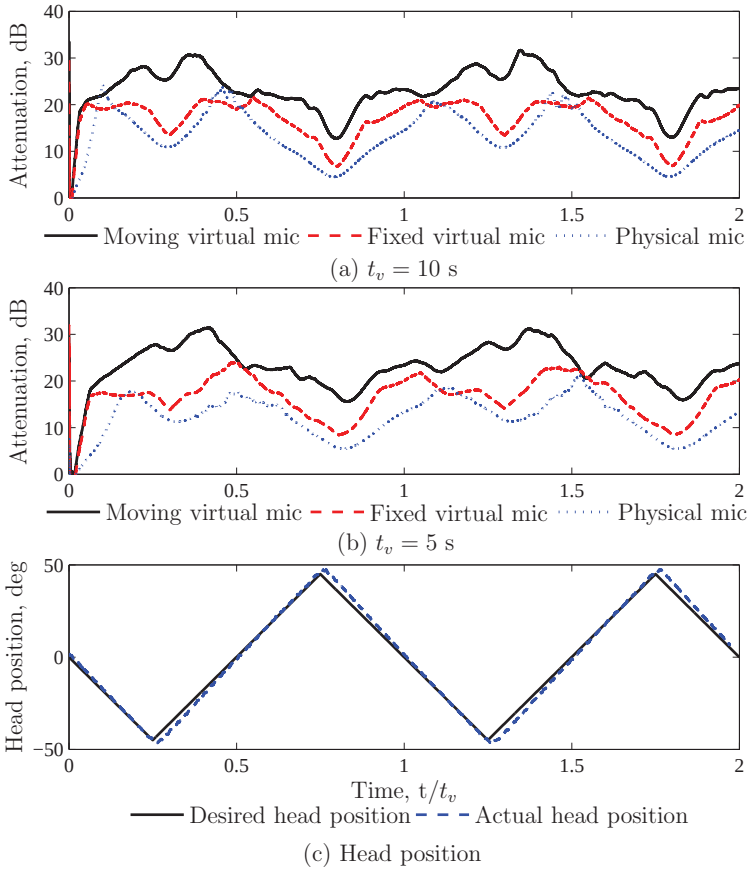

Figure 4.16: Tonal attenuation achieved at the 525 Hz resonance with the adaptive LMS moving virtual microphone technique for a three-dimensional sound field when $M_a = 3$ physical microphones are in triangular configuration. Control profiles are shown for active noise control at the moving virtual microphone, a virtual microphone spatially fixed at $\theta = 0°$, and the physical microphone, for a period of rotation (a) $t_v = 10$ s; (b) $t_v = 5$ s; and (c) head position.

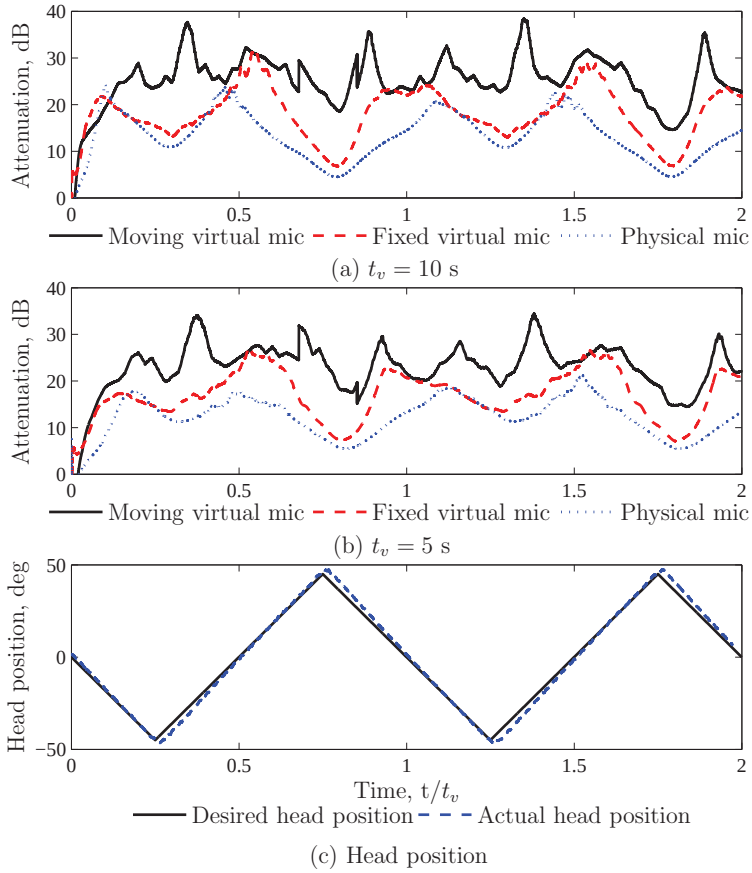

Figure 4.17: Tonal attenuation achieved at the 525 Hz resonance with the adaptive LMS moving virtual microphone technique for a three-dimensional sound field when $M_a = 4$ physical microphones are in tetrahedral configuration. Control profiles are shown for active noise control at the moving virtual microphone, a virtual microphone spatially fixed at $\theta = 0°$, and the physical microphone, for a period of rotation (a) $t_v = 10$ s; (b) $t_v = 5$ s; and (c) head position.

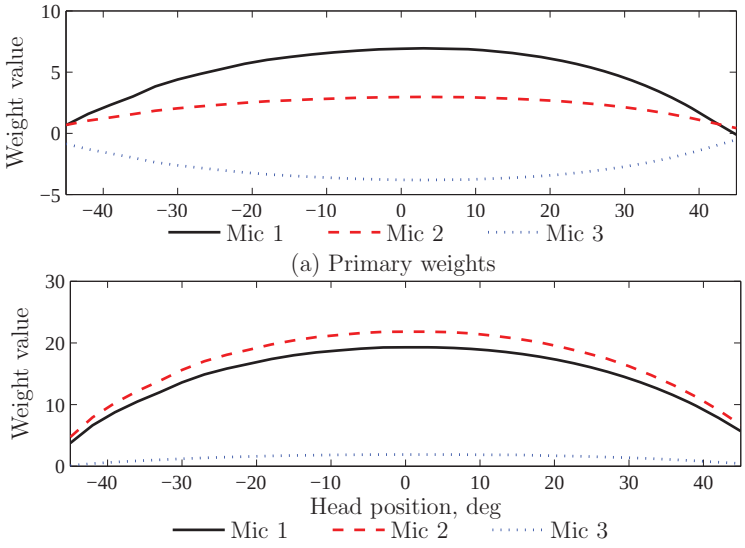

(a) Primary weights

(b) Secondary weights

Figure 4.18: Physical microphone weights for the adaptive LMS moving virtual microphone technique for a three-dimensional sound field at the 525 Hz resonance when the $M_a = 3$ physical microphones are in linear perpendicular configuration.

in tetrahedral formation results in the most accurate estimate of the moving virtual error signal and achieves the greatest attenuation at the moving virtual location.

Figs. 4.18 - 4.21 show the real valued physical microphone weights estimated with the adaptive LMS moving virtual microphone technique at the 525 Hz resonance. The physical sensor weights are given for $M_a = 3$ physical microphones in linear perpendicular formation, $M_a = 3$ physical microphones in linear parallel formation, $M_a = 3$ physical microphones in triangular formation and $M_a = 4$ physical microphones in tetrahedral formation respectively. The primary weights are shown in part (a) of Figs. 4.18 - 4.21, while the weights for the secondary sound field are shown in part (b) of Figs. 4.18 - 4.21 for head positions between $\theta_h = -45°$ and $\theta_h = 45°$.

The primary and secondary physical sensor weights for $M_a = 3$ physical microphones in linear perpendicular and parallel formation are very large, as seen in Figs. 4.18 and 4.19. This indicates that the estimation problem is poorly conditioned for these configurations of physical sensors. In comparison, the primary and secondary physical sensor weights for $M_a = 3$ physical microphones in triangular configuration and $M_a = 4$ physical microphones in tetrahedral configuration are much smaller, as seen in Figs. 4.20 and 4.21, indicating that the conditioning of the estimation problem is good in these cases. Such a result is to be expected given that

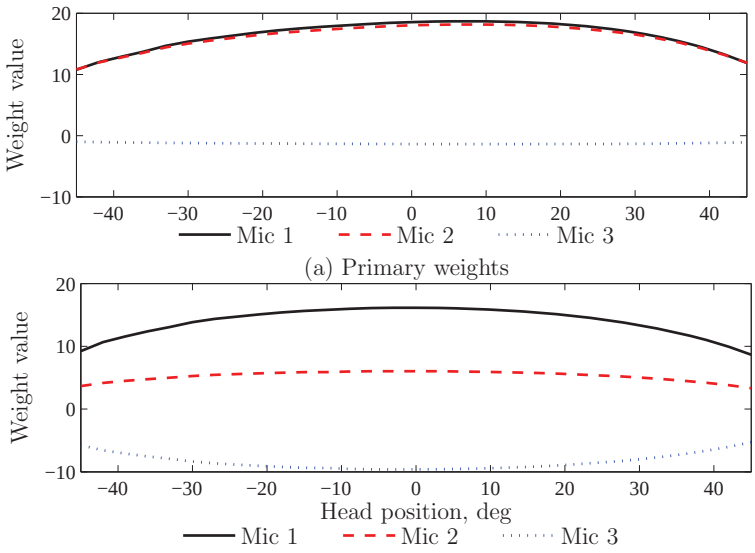

(a) Primary weights

(b) Secondary weights

Figure 4.19: Physical microphone weights for the adaptive LMS moving virtual microphone technique for a three-dimensional sound field at the 525 Hz resonance when the $M_a = 3$ physical microphones are in linear parallel configuration.

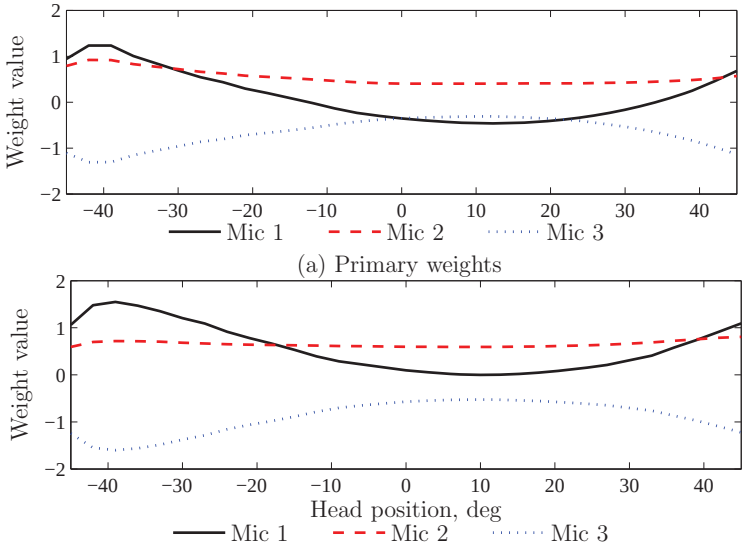

(a) Primary weights

(b) Secondary weights

Figure 4.20: Physical microphone weights for the adaptive LMS moving virtual microphone technique for a three-dimensional sound field at the 525 Hz resonance when the $M_a = 3$ physical microphones are in triangular configuration.

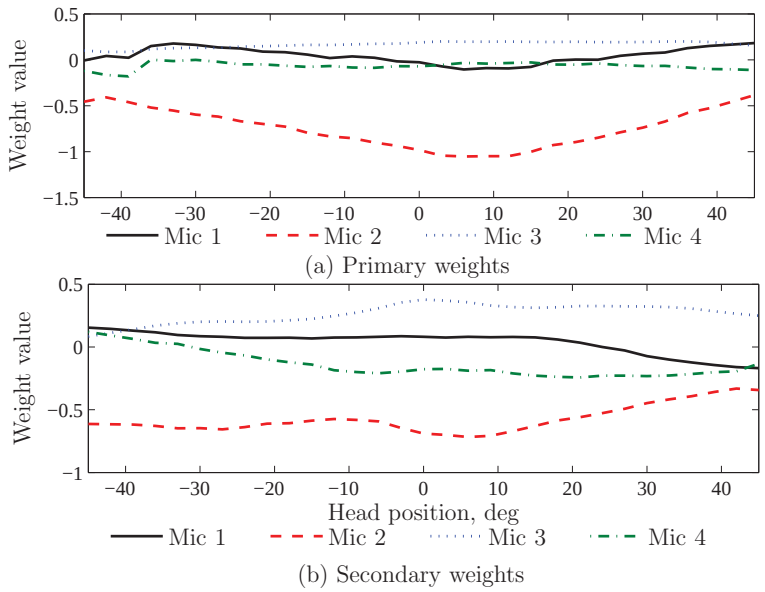

Figure 4.21: Physical microphone weights for the adaptive LMS moving virtual microphone technique for a three-dimensional sound field at the 525 Hz resonance when the $M_a = 4$ physical microphones are in tetrahedral configuration.

the three-dimensional physical sensor configurations should more accurately model the three-dimensional sound field than the one-dimensional physical sensor configurations. The tetrahedral configuration of $M_a = 4$ physical sensors has the smallest weight values indicating that the estimation problem is best conditioned for this arrangement of physical sensors. For the configurations tested, arranging $M_a = 4$ physical microphones in tetrahedral configuration therefore results in the most accurate estimate of the moving virtual error signal and the greatest attenuation at the moving virtual location.

Table 4.3 gives the time average and standard deviation of the attenuation achieved at the moving virtual location for the four different physical sensor configurations. Results are shown at the 525 Hz resonance for active noise control at the moving virtual microphone, a fixed virtual microphone located at the ear of the artificial head when $\theta_h = 0°$, and the physical microphone. Table 4.3 shows that for all physical sensor configurations and both periods of head rotation, minimising the moving virtual error signal achieves the greatest attenuation at the moving virtual location. Table 4.3 shows that arranging $M_a = 4$ physical microphones in tetrahedral formation generates the best control performance at the ear of the rotating artificial head. Minimising the moving virtual error signal with this configuration of physical sensors provides up to an additional 5 dB of attenuation at the ear of the

Table 4.3: Time average and standard deviation (in parentheses) of the attenuation in dB achieved at the moving virtual location at the 525 Hz resonance with the adaptive LMS moving virtual microphone technique for a three-dimensional sound field. Tabulated results are given for active noise control at the moving virtual microphone, a fixed virtual microphone located at the ear of the artificial head when $\theta_h = 0°$, and the physical microphone.

Physical sensor configuration	t_v s	Moving virtual mic	Fixed virtual mic	Physical mic
$M_a = 3$ physical microphones	10	20.2(5.2)	17.3(4.8)	11.8(5.9)
in linear perpendicular formation	5	19.8(5.0)	17.1(5.1)	13.2(5.5)
$M_a = 3$ physical microphones	10	20.6(6.3)	16.7(5.1)	13.1(5.6)
in linear parallel formation	5	19.8(6.8)	17.5(5.1)	11.7(5.7)
$M_a = 3$ physical microphones	10	22.8(4.5)	16.9(4.7)	13.2(5.4)
in triangular formation	5	22.9(4.8)	16.5(4.3)	12.1(4.9)
$M_a = 3$ physical microphones	10	25.2(5.1)	17.9(5.6)	13.2(5.6)
in tetrahedral formation	5	23.1(5.4)	16.8(6.2)	12.1(4.6)

rotating artificial head compared to the other physical sensor configurations. With $M_a = 4$ physical microphones in tetrahedral formation, active noise control at the moving virtual microphone provides up to an additional 7.3 dB of attenuation at the moving virtual location compared to active noise control at the fixed virtual microphone. Minimising the moving virtual error signal achieves up to an additional 12 dB of attenuation at the moving virtual location compared to minimising the fixed physical error signal.

As expected, comparing parts (a) and (b) of Figs. 4.14 - 4.17 shows that when the period of head rotation is reduced, the control performance reduces. Table 4.3 shows a decrease in the attenuation achieved at the moving virtual location and an increase in the standard deviation with a decrease in the period of head rotation. As already stated, this is because it takes a finite time for the controlled sound field to stabilise, so once the period of head rotation nears the reverberation time of the cavity, the control performance is compromised.

The performance of the adaptive LMS moving virtual microphone technique off resonance at 510 Hz, with $M_a = 4$ physical microphones in tetrahedral formation (chosen for its high performance), is shown in Fig. 4.22. Control profiles are shown for active noise control at the moving virtual microphone, a fixed virtual microphone located at the ear of the artificial head when $\theta_h = 0°$, and a physical microphone 4

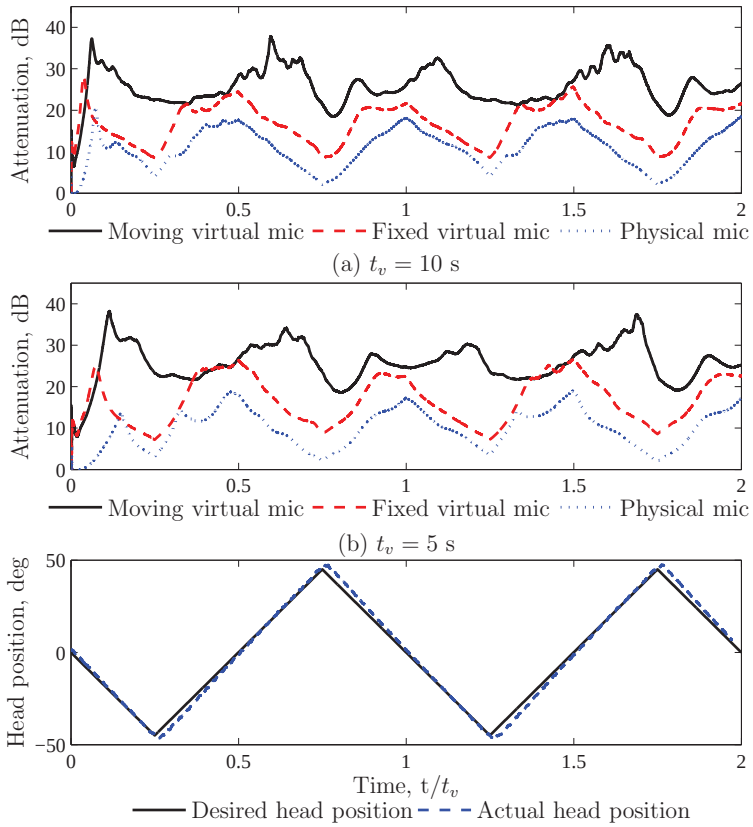

Figure 4.22: Tonal attenuation achieved off resonance at 510 Hz with the adaptive LMS moving virtual microphone technique for a three-dimensional sound field when $M_a = 4$ physical microphones are in tetrahedral configuration. Control profiles are shown for active noise control at the moving virtual microphone, a virtual microphone spatially fixed at $\theta = 0°$, and the physical microphone, for a period of rotation (a) $t_v = 10$ s; (b) $t_v = 5$ s; and (c) head position.

cm from the ear when $\theta_h = 0°$. The control performance at the ear of the rotating artificial head is shown for the period of head rotation of $t_v = 10$ s in Fig. 4.22 (a) and $t_v = 5$ s in Fig. 4.22 (b). A detailed description of this figure is given in Appendix B.2.

Table 4.4 gives the time average and standard deviation of the attenuation achieved at the moving virtual location with the adaptive LMS moving virtual microphone technique when $M_a = 4$ physical microphones are arranged in tetrahedral formation. Tabulated results are given for active noise control at the moving virtual microphone, a fixed virtual microphone located at the ear of the artificial head when $\theta_h = 0°$, and the physical microphone.

Table 4.4: Time average and standard deviation (in parentheses) of the attenuation in dB achieved at the moving virtual location with the adaptive LMS moving virtual microphone technique for a three-dimensional sound field when $M_a = 4$ physical microphones are arranged in tetrahedral formation. Results achieved in a modified sound field are highlighted in grey. Tabulated results are given for active noise control at the moving virtual microphone, a fixed virtual microphone located at the ear of the artificial head when $\theta = 0°$ and the physical microphone.

t_v s	525 Hz			510 Hz		
	Moving virtual mic	Fixed virtual mic	Physical mic	Moving virtual mic	Fixed virtual mic	Physical mic
10	25.2(5.1)	17.9(5.6)	13.2(5.6)	24.6(5.3)	16.7(4.6)	10.7(4.7)
5	23.1(5.4)	16.8(6.2)	12.1(4.6)	24.1(5.8)	16.6(5.7)	9.7(4.7)
10	18.3(6.1)	16.4(6.6)	11.4(6.7)	17.1(5.3)	13.3(5.1)	9.6(5.4)
5	17.8(5.1)	14.1(6.5)	9.3(5.6)	16.8(4.2)	11.9(6.0)	7.5(4.6)

Fig. 4.22 demonstrates that off resonance, minimising the moving virtual error signal achieves the greatest attenuation at the moving virtual location compared to minimising the fixed virtual error signal or the physical error signal. Table 4.4 shows that active noise control at the moving virtual microphone provides up to an additional 7.9 dB of attenuation off resonance compared to active noise control at the fixed virtual microphone. Minimising the moving virtual error signal achieves up to an additional 14.4 dB of attenuation at the moving virtual location compared to minimising the fixed physical error signal.

As expected, comparing Figs. 4.17 and 4.22 and the average attenuations at the two excitation frequencies in Table 4.4 demonstrates that reduced control performance is achieved off resonance. This is because a number of modes contribute to the cavity response when the primary noise disturbance is off resonance. Comparing the average attenuations at the two periods of head motion in Table 4.4 shows that as the period of head rotation decreases, the average attenuation achieved at the moving virtual location decreases and the standard deviation increases. As previously stated, this is because it takes a finite time for the controlled sound field to stabilise, so once the period of head rotation nears the reverberation time of the cavity, the control performance is compromised.

4.3.2.1 Robustness of the adaptive LMS moving virtual microphone technique for a three-dimensional sound field

The adaptive LMS moving virtual microphone technique computes an estimate of the pressure at the moving virtual location by interpolating the virtual error signals at a number of spatially fixed virtual locations estimated using the adaptive LMS virtual microphone technique (Cazzolato, 2002). To estimate the virtual error signals at the spatially fixed virtual locations, the adaptive LMS virtual microphone technique requires models of the physical secondary transfer functions and the primary and secondary weights at the spatially fixed virtual locations. Models of the physical secondary transfer functions and the primary and secondary weights at the spatially fixed virtual locations are obtained prior to active noise control in a preliminary identification stage. The adaptive LMS moving virtual microphone technique is therefore not robust to changes in the sound field that may alter the transfer functions between the error sensors and the sources. To investigate the robustness of this moving virtual sensing method, the performance of the active noise control system in generating a zone of quiet at the moving virtual location was examined after modifying the sound field, as in Section 4.3.1.1. Firstly, the preliminary identification stage was conducted in which the required transfer functions were measured and the physical sensor weights were calculated for the rotating artificial head and the physical sensors being located at a certain position within the cavity. Once the preliminary identification stage was complete, the rotating artificial head and the physical sensors were moved 3 cm ($\approx 5\%$ of λ) within the cavity to a new position, while ensuring the relative arrangement of the physical and virtual sensors remained constant. Changing the position of the experimental equipment within the cavity is equivalent to a significant shift in the sound field. The performance of the active noise control system in generating a zone of quiet at the ear of the rotating artificial head was then investigated at this new position using the transfer functions and the physical sensor weights calculated at the original position in the preliminary identification stage.

It was shown in the previous section that arranging $M_a = 4$ physical microphones in tetrahedral formation results in the most accurate estimate of the error signal at the moving virtual location and the greatest control performance at the ear of the rotating artificial head. Therefore, the robustness of the adaptive LMS moving virtual microphone technique is only examined for this configuration of physical sensors. Figs. 4.23 and 4.24 show the performance of the active noise control system

in generating a zone of quiet at the ear of the rotating artificial head with the adaptive LMS moving virtual microphone technique after modifying the sound field. The attenuation achieved at the moving virtual location is shown at the 525 Hz resonance and off resonance at 510 Hz in Figs. 4.23 and 4.24 respectively. Control profiles are shown for active noise control at the moving virtual microphone, a fixed virtual microphone located at the ear of the artificial head when $\theta_h = 0°$, and the fixed physical microphone. The control performance at the ear of the artificial head is shown for the period of head rotation being $t_v = 10$ s in part (a) of Figs. 4.23 and 4.24, and $t_v = 5$ s in part (b) of Figs. 4.23 and 4.24. Part (c) of Figs. 4.23 and 4.24 shows the desired trajectory of the artificial head and of the moving virtual microphone, in degrees, compared to the actual controlled head position. A detailed description of each of these figures is given in Appendix B.2.1.

The time average and standard deviation of the attenuation achieved with the adaptive LMS moving virtual microphone technique after modification of the sound field are given in the grey shaded section of Table 4.4. Tabulated results are given for active noise control at the moving virtual microphone, a fixed virtual microphone located at the ear of the artificial head when $\theta_h = 0°$, and the physical microphone, for the two excitation frequencies of 525 Hz and 510 Hz and for the period of head rotation being $t_v = 10$ s and $t_v = 5$ s.

The control profiles in Figs. 4.23 and 4.24 demonstrate that minimising the moving virtual error signal achieves the best control performance at the moving virtual location even after modification of the sound field. Table 4.4 states that active noise control at the moving virtual microphone after modifying the sound field provides up to an additional 4.9 dB of attenuation at the moving virtual location compared to active noise control at the fixed virtual microphone. After modifying the sound field, minimising the moving virtual error signal achieves up to an additional 9.3 dB of attenuation at the moving virtual location compared to minimising the fixed physical error signal. There is, however, a significant reduction in control performance when active noise control is performed in a modified sound field compared to in an unmodified sound field. Table 4.4 indicates that the attenuation achieved by minimising the moving virtual error signal is reduced by up to 7.5 dB when active noise control is performed in the modified sound field. Minimising the fixed virtual error signal after modifying the sound field reduces the attenuation achieved at the moving virtual location by up to 4.7 dB. This indicates a lack of robustness in the three-dimensional adaptive LMS moving virtual microphone technique and that this moving virtual sensing method is adversely affected by changes in the sound field

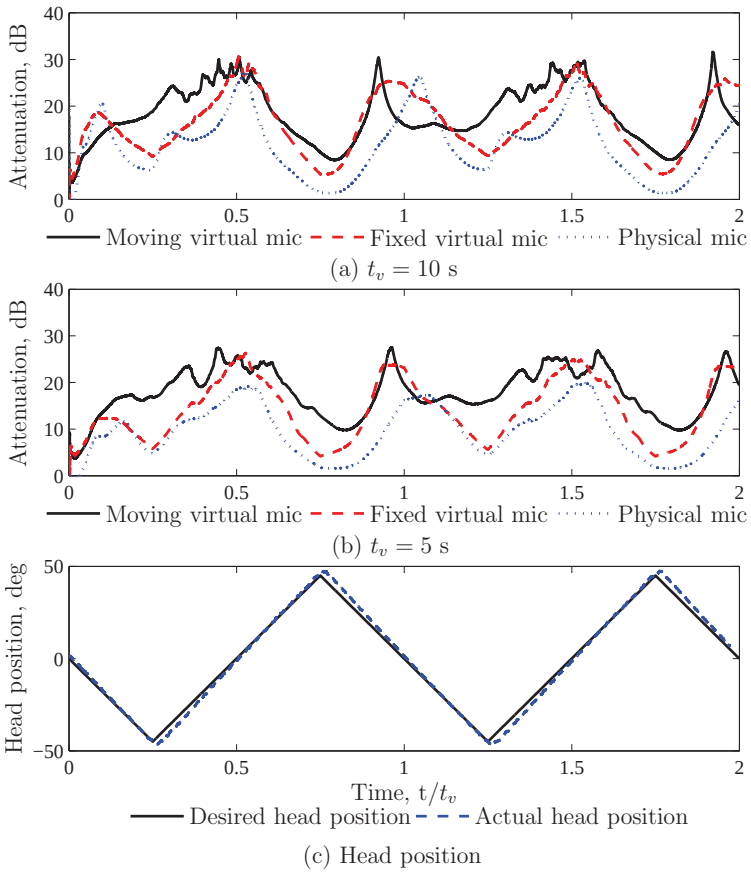

(a) $t_v = 10$ s

(b) $t_v = 5$ s

(c) Head position

Figure 4.23: Tonal attenuation achieved at the 525 Hz resonance with the adaptive LMS moving virtual microphone technique for a three-dimensional sound field after modifying the sound field. Results are shown for $M_a = 4$ physical microphones arranged in tetrahedral formation. Control profiles are shown for active noise control at the moving virtual microphone, a virtual microphone spatially fixed at $\theta = 0°$, and the physical microphone, for a period of rotation (a) $t_v = 10$ s; (b) $t_v = 5$ s; and (c) head position.

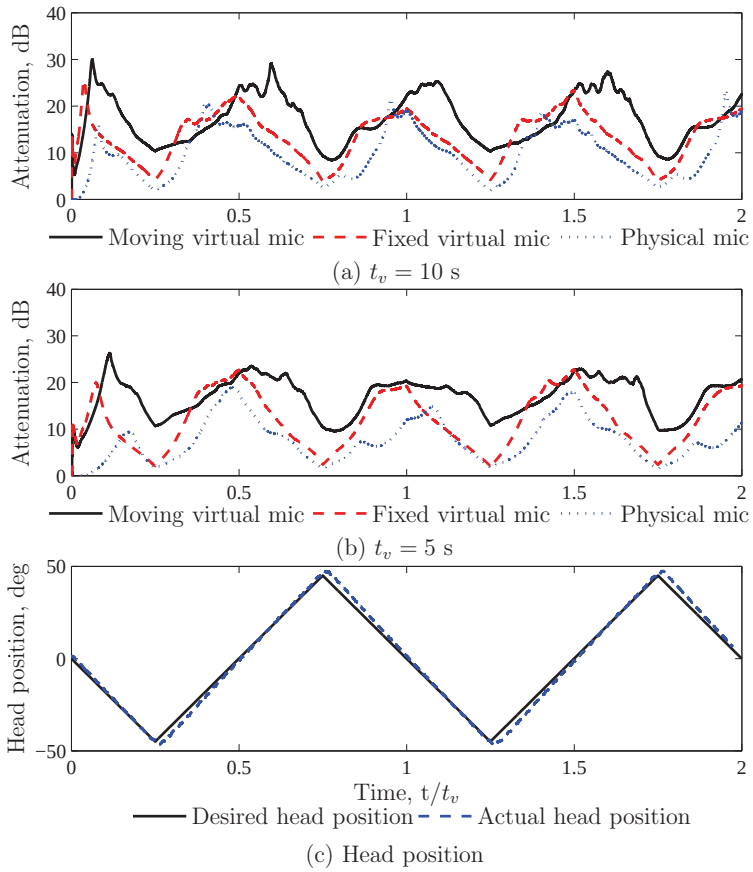

Figure 4.24: Tonal attenuation achieved off resonance at 510 Hz with the adaptive LMS moving virtual microphone technique for a three-dimensional sound field after modifying the sound field. Results are shown for $M_a = 4$ physical microphones arranged in tetrahedral formation. Control profiles are shown for active noise control at the moving virtual microphone, a virtual microphone spatially fixed at $\theta = 0°$, and the physical microphone, for a period of rotation (a) $t_v = 10$ s; (b) $t_v = 5$ s; and (c) head position.

that alter the transfer functions between the error sensors and the sources.

4.3.3 The Stochastically Optimal Tonal Diffuse Field (SOTDF) moving virtual sensing method for a three-dimensional sound field

The average attenuation achieved at the moving virtual location with the SOTDF moving virtual sensing method at the 525 Hz resonance is shown in Figs. 4.25 - 4.27. These figures give the control performance at the moving virtual location for the virtual quantities being estimated using the measured pressure and pressure gradient at a point (physical sensor arrangement shown in Fig. 4.7), the measured pressures at two points (physical sensor arrangement shown in Fig. 4.7) and the measured pressures at three points (physical sensor arrangement shown in Fig. 4.8) respectively. The results of real-time experimental control with the SOTDF moving virtual sensing method have been generated by averaging the results over a number of data sets. This is because this moving virtual sensing method gives a stochastically optimal estimate of the virtual error signal at the moving virtual location. To obtain a number of data sets to provide the spatial average, the rotating artificial head and the sensors were located at ten different positions within the cavity while ensuring the relative arrangement of the sensors and the rotating artificial head remained constant. The control profiles in Figs. 4.25 - 4.27 have been generated by averaging the results of active noise control at the 10 different locations. In Figs. 4.25 - 4.27, the average control profiles are shown for active noise control at the moving virtual microphone, a fixed virtual microphone located at the ear of the rotating artificial head when $\theta_h = 0°$, and the fixed physical microphone located 4 cm from the ear when $\theta_h = 0°$. The average control performance at the ear of the rotating artificial head is shown for the period of head rotation being $t_v = 10$ s in part (a) of Figs. 4.25 - 4.27 and $t_v = 5$ s in part (b) of Figs. 4.25 - 4.27. Part (c) of Figs. 4.25 - 4.27 shows the desired trajectory of the artificial head and of the moving virtual microphone, in degrees, compared to the actual controlled head position. Again, the transient behaviour seen in Figs. 4.25 - 4.27 at time $t/t_v = 0$ s for both $t_v = 5$ s and $t_v = 10$ s, is caused by the controller initialising. A detailed description of each of these figures is given in Appendix B.3.

The control profiles in Figs. 4.25 - 4.27 demonstrate that minimising the moving virtual error signal estimated using the SOTDF moving virtual sensing method generates the best control performance at the ear of the rotating artificial head

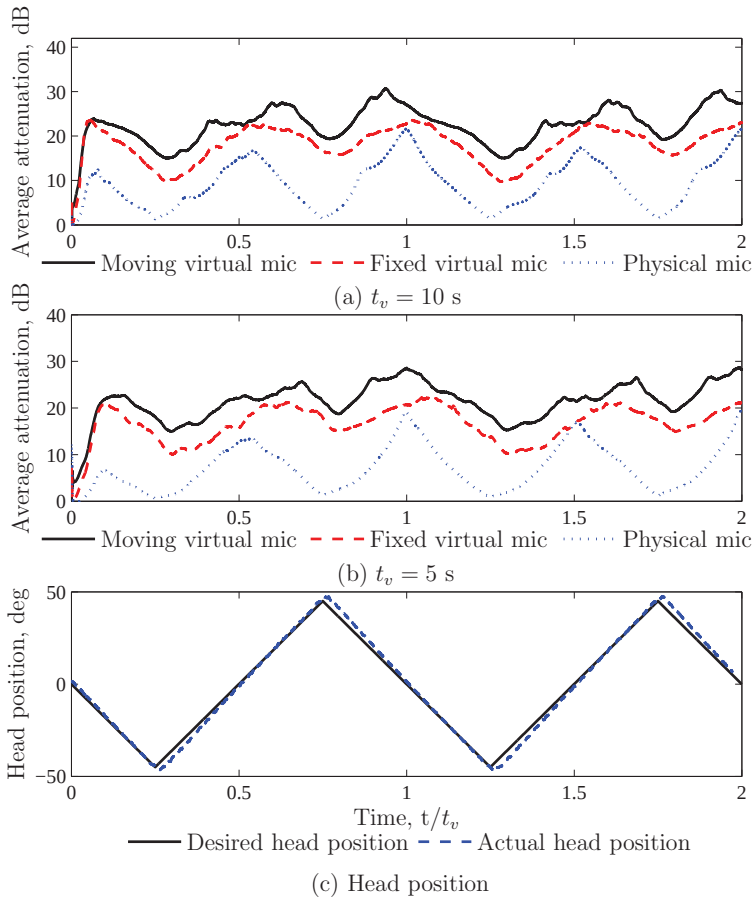

(a) $t_v = 10$ s

(b) $t_v = 5$ s

(c) Head position

Figure 4.25: The average tonal attenuation achieved at the 525 Hz resonance with the SOTDF moving virtual sensing method for a three-dimensional sound field using the measured pressure and pressure gradient at a point (physical sensor arrangement shown in Fig. 4.7). Control profiles are shown for active noise control at the moving virtual microphone, a virtual microphone spatially fixed at $\theta = 0°$, and the physical microphone, for a period of rotation (a) $t_v = 10$ s; (b) $t_v = 5$ s; and (c) head position.

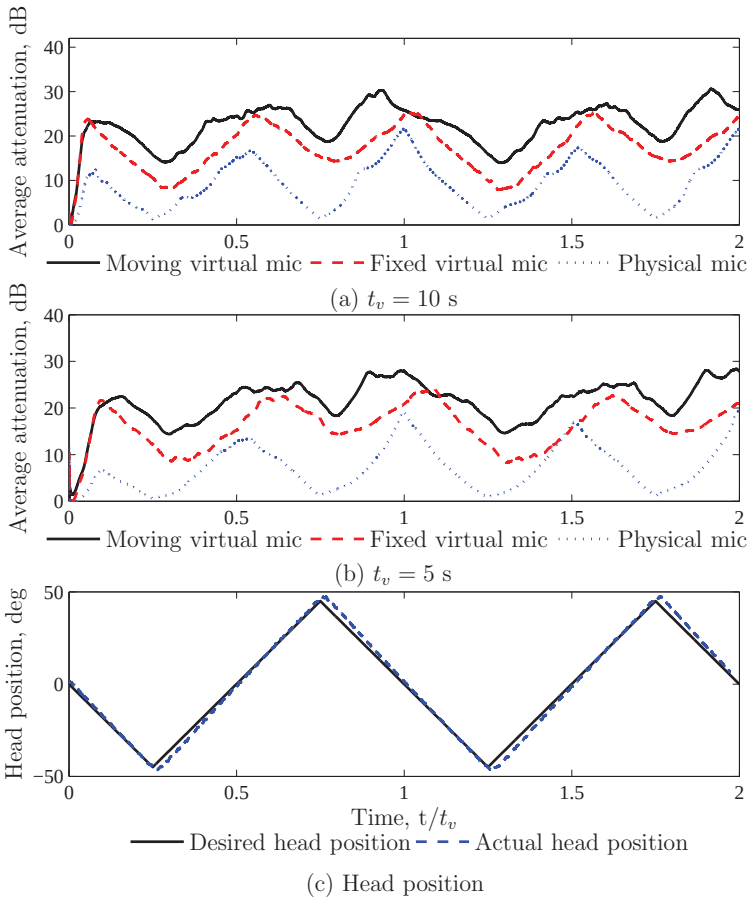

Figure 4.26: The average tonal attenuation achieved at the 525 Hz resonance with the SOTDF moving virtual sensing method for a three-dimensional sound field using the measured pressures at two points (physical sensor arrangement shown in Fig. 4.7). Control profiles are shown for active noise control at the moving virtual microphone, a virtual microphone spatially fixed at $\theta = 0°$, and the physical microphone, for a period of rotation (a) $t_v = 10$ s; (b) $t_v = 5$ s; and (c) head position.

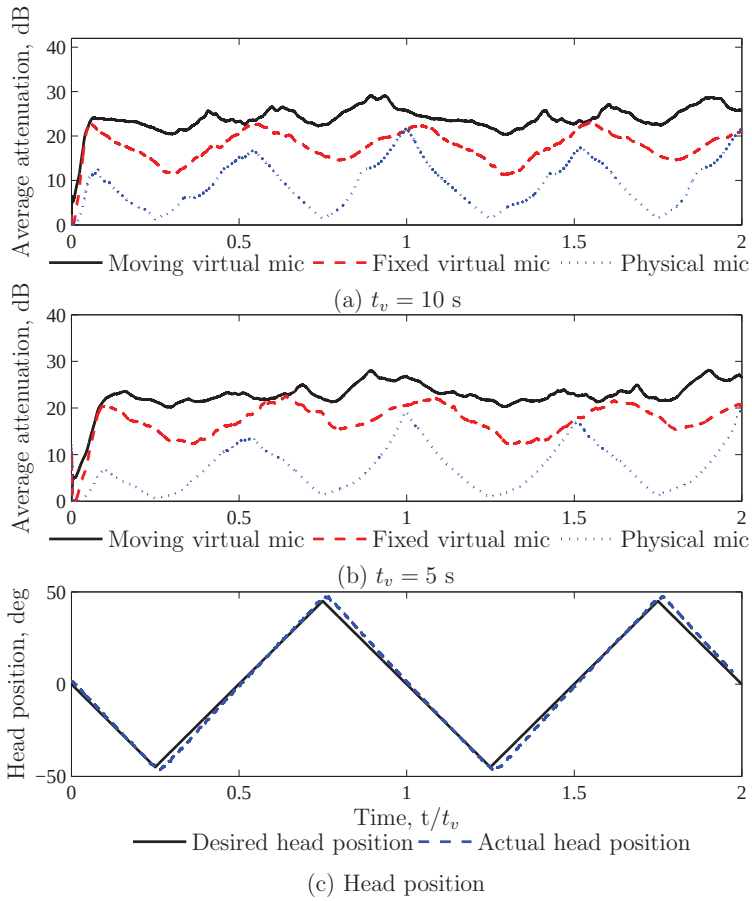

Figure 4.27: The average tonal attenuation achieved at the 525 Hz resonance with the SOTDF moving virtual sensing method for a three-dimensional sound field using the measured pressures at three points (physical sensor arrangement shown in Fig. 4.8). Control profiles are shown for active noise control at the moving virtual microphone, a virtual microphone spatially fixed at $\theta = 0°$, and the physical microphone, for a period of rotation (a) $t_v = 10$ s; (b) $t_v = 5$ s; and (c) head position.

regardless of the number or the arrangement of the physical sensors. Comparing Figs. 4.25 - 4.27 shows that using three physical microphones in a triangular arrangement around the rotating artificial head to estimate the moving virtual error signal achieves the greatest control performance at the moving virtual location. While peak levels of attenuation are achieved when the virtual error signal is estimated using the measured pressure and pressure gradient at a point, using the measured pressures at three points generates the smoothest control profile. A smooth control profile is desirable as a significant change in sound pressure level with head rotation may be more irritating than the original disturbance alone.

Table 4.5 gives the time average and standard deviation of the attenuation achieved at the 525 Hz resonance with the three different physical sensor configurations. Results are shown for active noise control at the moving virtual microphone, a fixed virtual microphone located at the ear of the artificial head when $\theta_h = 0°$ and the physical microphone. For all three physical sensor configurations and both periods of head rotation, Table 4.5 shows that minimising the moving virtual error signal achieves the greatest attenuation at the moving virtual location. Table 4.5 also confirms that using the measured pressures at three points to estimate the moving virtual error signal generates the best control performance at the ear of the rotating artificial head. An additional 1.5 dB of attenuation is achieved when this configuration of physical sensors is used to estimate the moving virtual error signal compared to using the other physical sensor configurations. The standard deviation of the attenuation is also significantly smaller when using the measured pressures at three points to estimate the moving virtual error signal, indicating a smaller variation in sound pressure level with head movement. Table 4.5 reveals that minimising the moving virtual error signal estimated using the measured pressures at three points provides up to an additional 6.3 dB of attenuation compared to minimising the fixed virtual error signal. Active noise control at the moving virtual microphone achieves up to an additional 15.6 dB of attenuation at the moving virtual location compared to active noise control at the fixed physical microphone.

As expected, comparing parts (a) and (b) of Figs. 4.25 - 4.27 shows that when the period of head rotation is reduced, the control performance reduces. Table 4.5 also shows a decrease in the attenuation and an increase in the standard deviation with a decrease in the period of head rotation. As previously explained, this is because it takes a finite time for the controlled sound field to stabilise, so once the period of head rotation nears the reverberation time of the cavity, the control performance is compromised.

Table 4.5: Time average and standard deviation (in parentheses) of the average attenuation in dB achieved at the moving virtual location at the 525 Hz resonance with the SOTDF moving virtual sensing method for a three-dimensional sound field. Tabulated results are given for active noise control at the moving virtual microphone, a fixed virtual microphone located at the ear of the artificial head when $\theta_h = 0°$ and the fixed physical microphone.

Physical sensor configuration	t_v s	Moving virtual mic	Fixed virtual mic	Physical mic
Using the measured pressure	10	22.4(4.2)	18.0(4.1)	9.1(5.3)
and pressure gradient at a point	5	21.4(4.3)	16.5(4.2)	7.1(4.8)
Using the measured pressures	10	22.4(4.5)	17.1(4.9)	9.2(4.3)
at two points	5	21.3(4.6)	16.1(4.7)	7.4(4.8)
Using the measured pressures	10	23.9(2.8)	17.6(3.4)	9.1(4.3)
at three points	5	22.7(3.2)	17.2(3.5)	7.1(4.8)

The individual control profiles generated at each of the 10 different cavity locations when the moving virtual error signal is minimised are given in Figs. 4.28 - 4.30. These figures show the attenuations achieved at the ear of the rotating artificial head at resonance, when the moving virtual error signal is estimated using the measured pressure and pressure gradient at a point, the measured pressures at two points, and the measured pressures at three points respectively. The average attenuation generated by averaging the results over the 10 data sets is also shown in black. The control profiles in Figs. 4.28 - 4.30 have a minimum attenuation level of 5 dB. This demonstrates that minimising the moving virtual error signal has not increased the original sound pressure level measured at the moving virtual location at any time during head motion at any of the 10 different cavity positions.

Figs. 4.31 - 4.33 show the individual control profiles generated at each of the 10 different cavity locations when the fixed virtual error signal is minimised. The attenuations achieved at the moving virtual location are shown for the fixed virtual error signal being estimated using the measured pressure and pressure gradient at a point, the measured pressures at two points, and the measured pressures at three points respectively. The average attenuation generated by averaging the results over the 10 data sets is also shown in black. The control profiles in Figs. 4.31 - 4.33 have a minimum attenuation level that falls below 0 dB. This demonstrates that at certain cavity positions, active noise control at the fixed virtual microphone has caused an increase in the original sound pressure level measured at the ear of the rotating

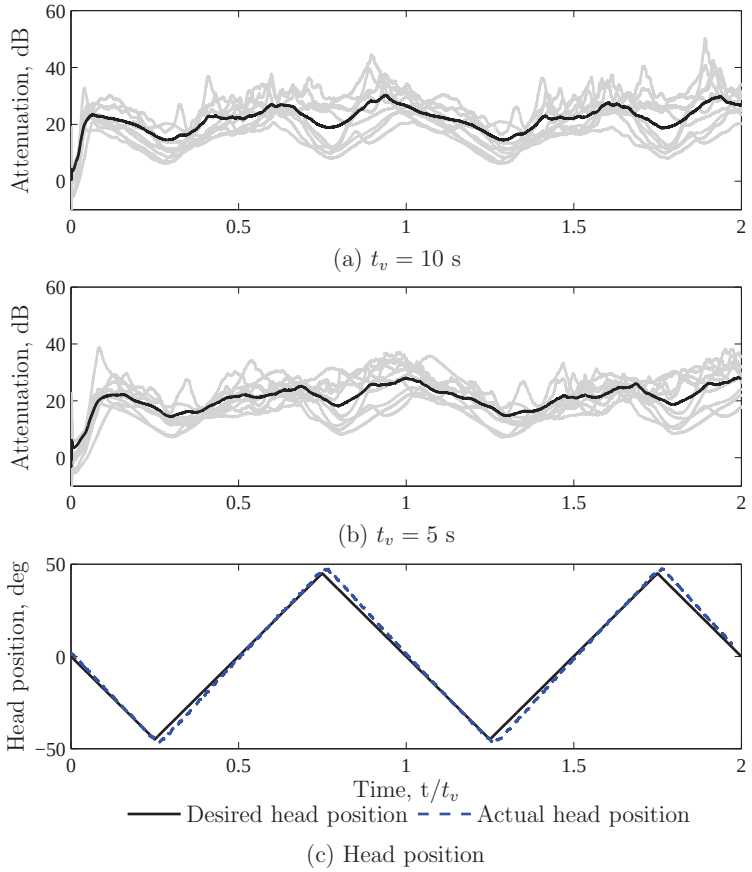

Figure 4.28: The 10 data set control profiles achieved at 525 Hz at the moving virtual location for active noise control at the moving virtual microphone with the SOTDF moving virtual sensing method for a three-dimensional sound field. The moving virtual error signal has been estimated using the measured pressure and pressure gradient at a point (physical sensor arrangement shown in Fig. 4.7). The average control profile is shown in black.

artificial head.

The experimental results presented in Figs. 4.25 - 4.27 show the performance of the SOTDF moving virtual sensing method in a sound field that is not perfectly diffuse. Active noise control at the moving virtual sensors provides improved attenuation at the ear of the rotating artificial head compared to minimising either the fixed virtual error signal or fixed physical error signal in a modally dense sound field. This demonstrates that stochastically optimal moving and fixed virtual sensors are suitable for use in a sound field that is not perfectly diffuse.

The performance of the SOTDF moving virtual sensing method in a modally dense sound field can be compared to diffuse field theory. Experimental control

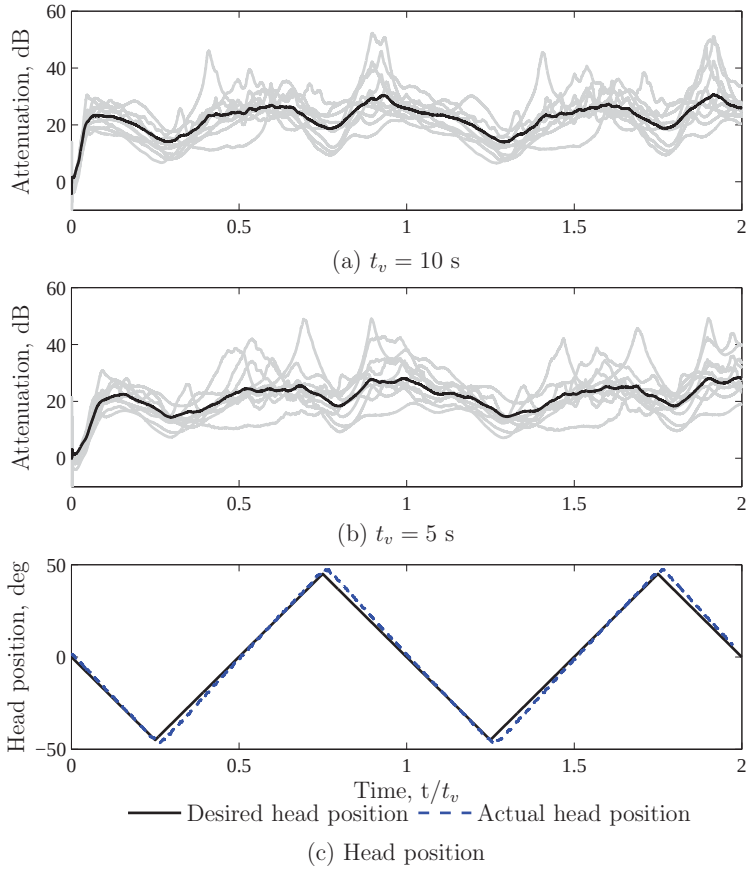

(a) $t_v = 10$ s

(b) $t_v = 5$ s

(c) Head position

Figure 4.29: The 10 data set control profiles achieved at 525 Hz at the moving virtual location for active noise control at the moving virtual microphone with the SOTDF moving virtual sensing method for a three-dimensional sound field. The moving virtual error signal has been estimated using the measured pressures at two points (physical sensor arrangement shown in Fig. 4.7). The average control profile is shown in black.

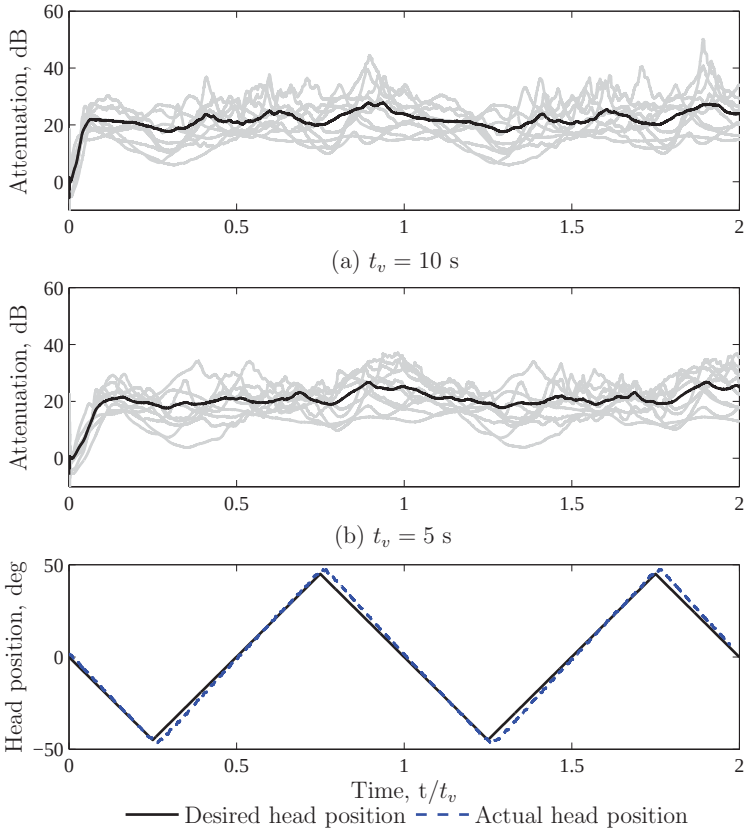

Figure 4.30: The 10 data set control profiles achieved at 525 Hz at the moving virtual location for active noise control at the moving virtual microphone with the SOTDF moving virtual sensing method for a three-dimensional sound field. The moving virtual error signal has been estimated using the measured pressures at three points (physical sensor arrangement shown in Fig. 4.8). The average control profile is shown in black.

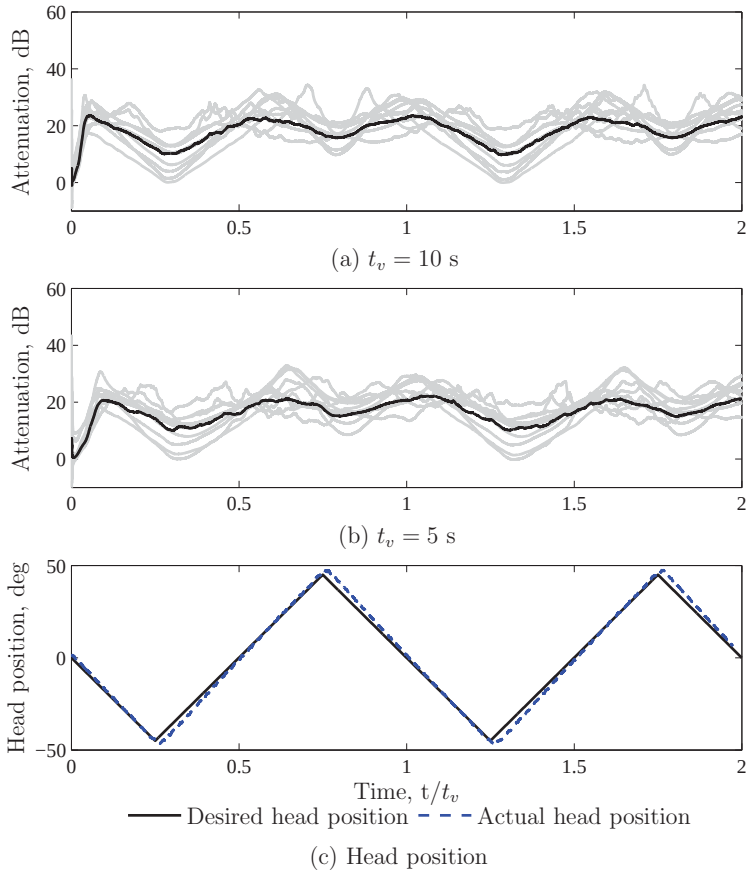

(a) $t_v = 10$ s

(b) $t_v = 5$ s

(c) Head position

Figure 4.31: The 10 data set control profiles achieved at 525 Hz at the moving virtual location for active noise control at the fixed virtual microphone with the SOTDF moving virtual sensing method for a three-dimensional sound field. The fixed virtual error signal has been estimated using the measured pressure and pressure gradient at a point (physical sensor arrangement shown in Fig. 4.7). The average control profile is shown in black.

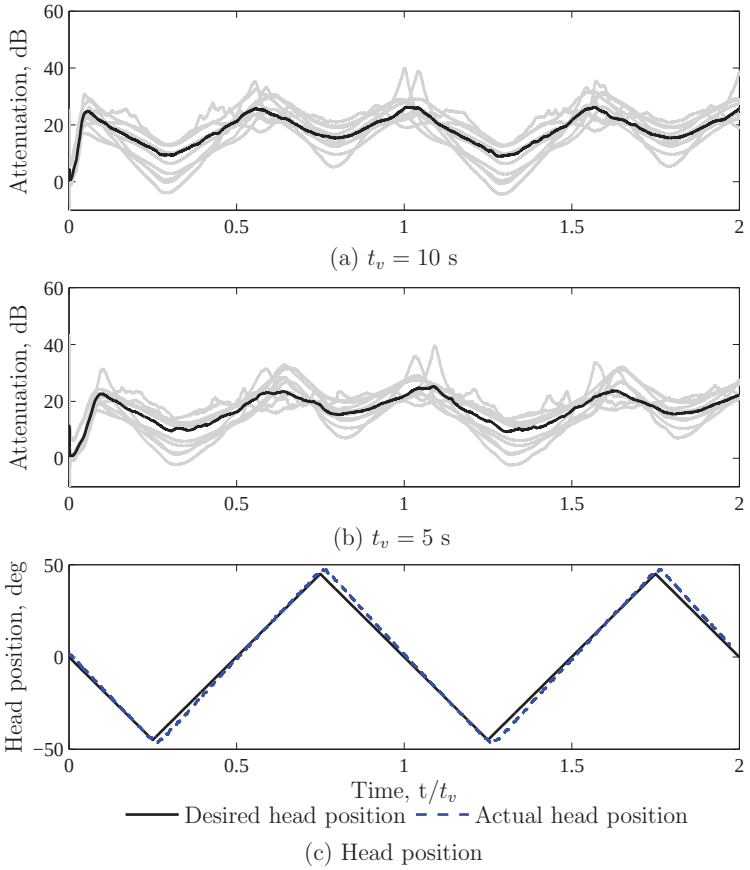

Figure 4.32: The 10 data set control profiles achieved at 525 Hz at the moving virtual location for active noise control at the fixed virtual microphone with the SOTDF moving virtual sensing method for a three-dimensional sound field. The fixed virtual error signal has been estimated using the measured pressures at two points (physical sensor arrangement shown in Fig. 4.7). The average control profile is shown in black.

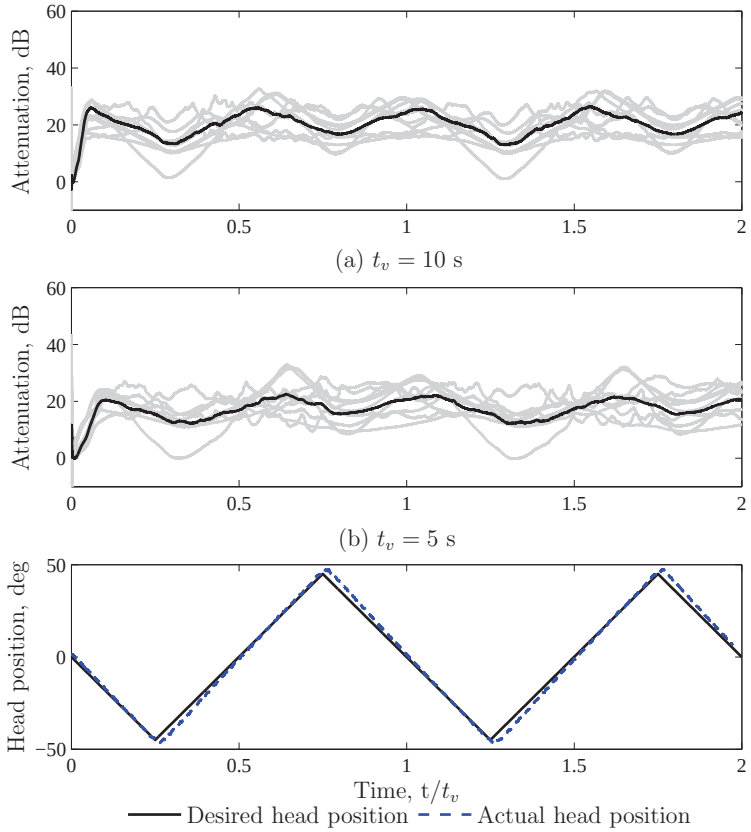

(a) $t_v = 10$ s

(b) $t_v = 5$ s

(c) Head position

Figure 4.33: The 10 data set control profiles achieved at 525 Hz at the moving virtual location for active noise control at the fixed virtual microphone with the SOTDF moving virtual sensing method for a three-dimensional sound field. The fixed virtual error signal has been estimated using the measured pressures at three points (physical sensor arrangement shown in Fig. 4.8). The average control profile is shown in black.

profiles for the relative change in mean squared pressure after control at the moving virtual microphone are shown in Figs. 4.34 - 4.36 together with the analytical expressions derived in Section 4.1.3. These figures compare the results of experimental control in a modally dense sound field at resonance to analytical expressions for the relative change in mean squared pressure after control in a diffuse sound field. The analytical and experimental control profiles are shown in Figs. 4.34 - 4.36 for the moving virtual error signal being estimated using the measured pressure and pressure gradient at a point, the measured pressures at two points, and the measured pressures at three points respectively. The analytical expressions for the relative change in mean squared pressure after control given in Eqs. (4.16), (4.18) and (4.36) are plotted in Figs. 4.34 - 4.36 respectively, for the 50th percentile value of $\alpha = 2$, as was found in Section 3.3. The experimental control profiles in Figs. 4.34 - 4.36 have been generated by averaging the results of active noise control at the 10 different cavity locations. The control performance at the ear of the rotating artificial head is shown for the period of head rotation of $t_v = 10$ s in part (a) of Figs. 4.34 - 4.36 and $t_v = 5$ s in part (b) of Figs. 4.34 - 4.36. Part (c) of Figs. 4.34 - 4.36 shows the desired trajectory of the artificial head and of the moving virtual microphone, in degrees, compared to the actual controlled head position.

Figs. 4.34 - 4.36 show that the experimental control profiles for the relative change in mean squared pressure in a modally dense sound field are similar to the analytical control profiles. This indicates that diffuse field theory can be used to predict the performance of the SOTDF moving virtual sensing method in a sound field that is not perfectly diffuse. Due to practical limitations, the experimental results were generated by averaging over only 10 data sets and this explains why the analytical expressions produce much smoother control profiles than the experimental data.

The performance of the SOTDF moving virtual sensing method off resonance at 510 Hz is shown in Fig. 4.37. In this figure, the moving and fixed virtual error signals have been estimated using the measured pressures at three points. This configuration of physical sensors was shown to generate the best control performance at the moving virtual location. Control profiles are shown for active noise control at the moving virtual microphone, a fixed virtual microphone located at the ear of the artificial head when $\theta_h = 0°$, and a fixed physical microphone 4 cm from the ear when $\theta_h = 0°$. The control performance at the ear of the rotating artificial head is shown for the period of head rotation of $t_v = 10$ s in Fig. 4.37 (a) and $t_v = 5$ s in Fig. 4.37 (b). Fig. 4.37 (c) shows the desired trajectory of the artificial head and of the moving virtual microphone, in degrees, compared to the actual controlled head

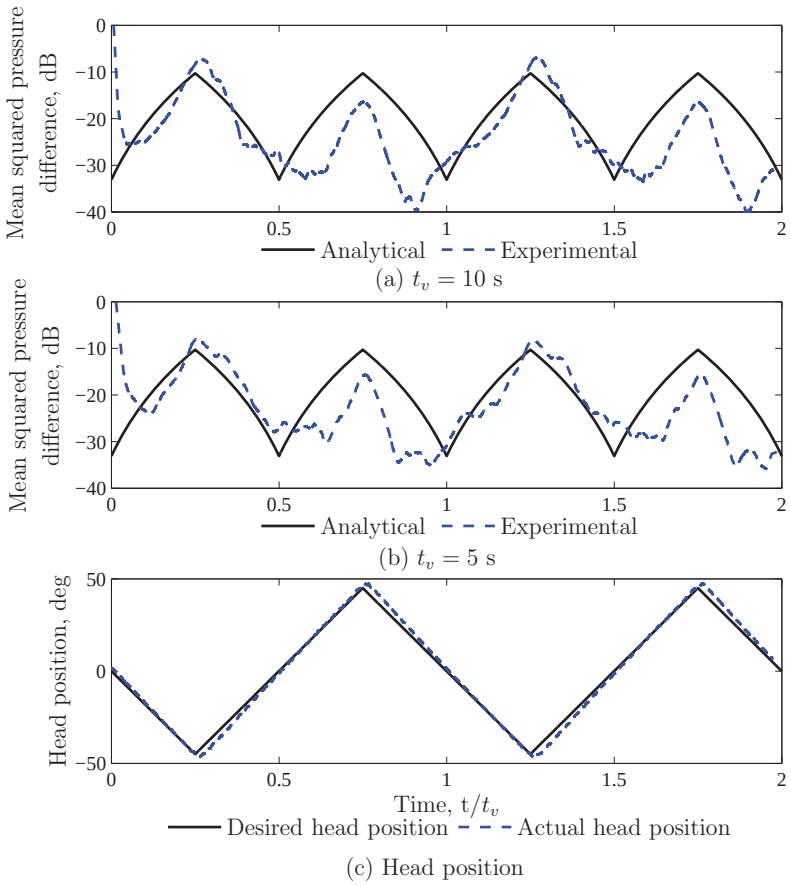

(a) $t_v = 10$ s

(b) $t_v = 5$ s

(c) Head position

Figure 4.34: The relative change in mean squared pressure achieved in analytical and experimental control at the 525 Hz resonance with the SOTDF moving virtual sensing method for a three-dimensional sound field using the measured pressure and pressure gradient at a point (physical sensor arrangement shown in Fig. 4.7). Control profiles are shown for active noise control at the moving virtual microphone, for a period of rotation (a) $t_v = 10$ s; (b) $t_v = 5$ s; and (c) head position.

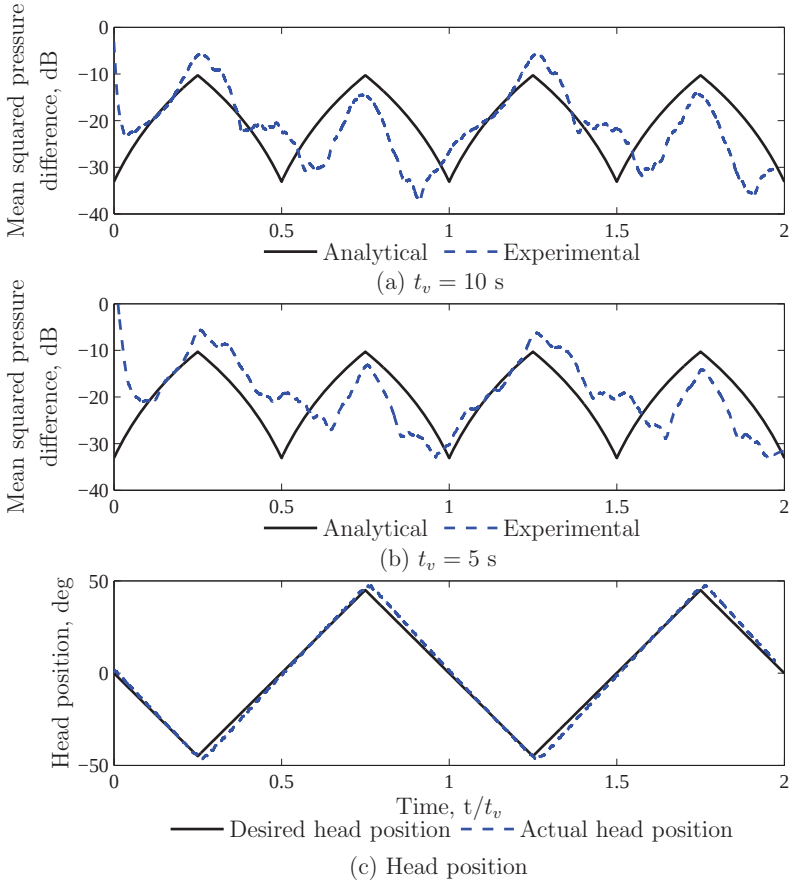

Figure 4.35: The relative change in mean squared pressure achieved in analytical and experimental control at the 525 Hz resonance with the SOTDF moving virtual sensing method for a three-dimensional sound field using the measured pressures at two points (physical sensor arrangement shown in Fig. 4.7). Control profiles are shown for active noise control at the moving virtual microphone, for a period of rotation (a) $t_v = 10$ s; (b) $t_v = 5$ s; and (c) head position.

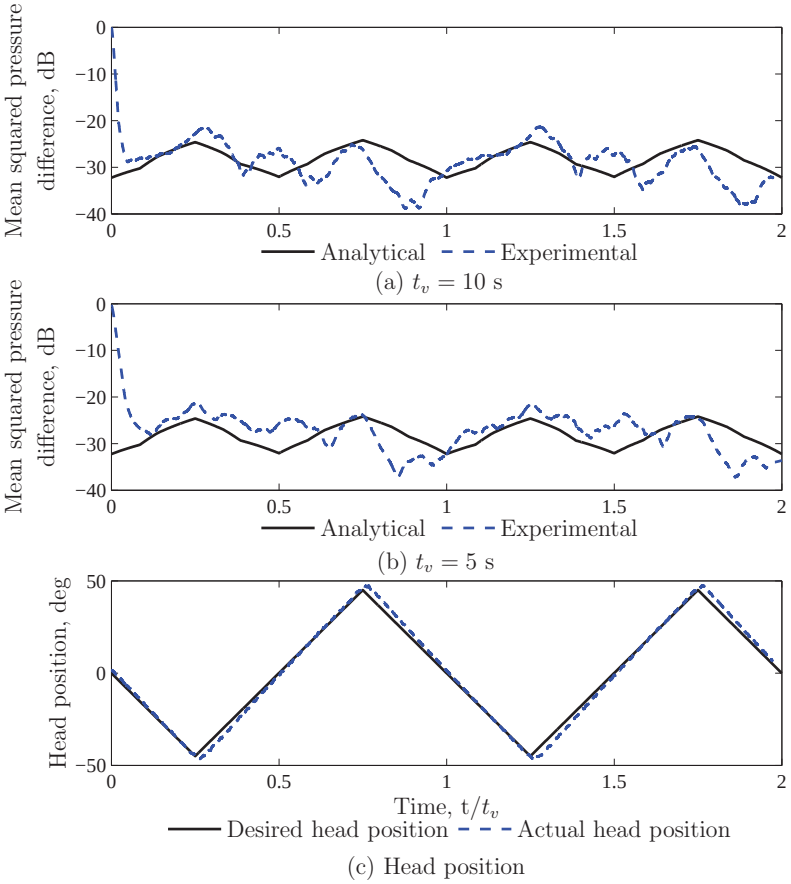

Figure 4.36: The relative change in mean squared pressure achieved in analytical and experimental control at the 525 Hz resonance with the SOTDF moving virtual sensing method for a three-dimensional sound field using the measured pressures at three points (physical sensor arrangement shown in Fig. 4.8). Control profiles are shown for active noise control at the moving virtual microphone, for a period of rotation (a) $t_v = 10$ s; (b) $t_v = 5$ s; and (c) head position.

position. A detailed description of this figure is given in Appendix B.3.

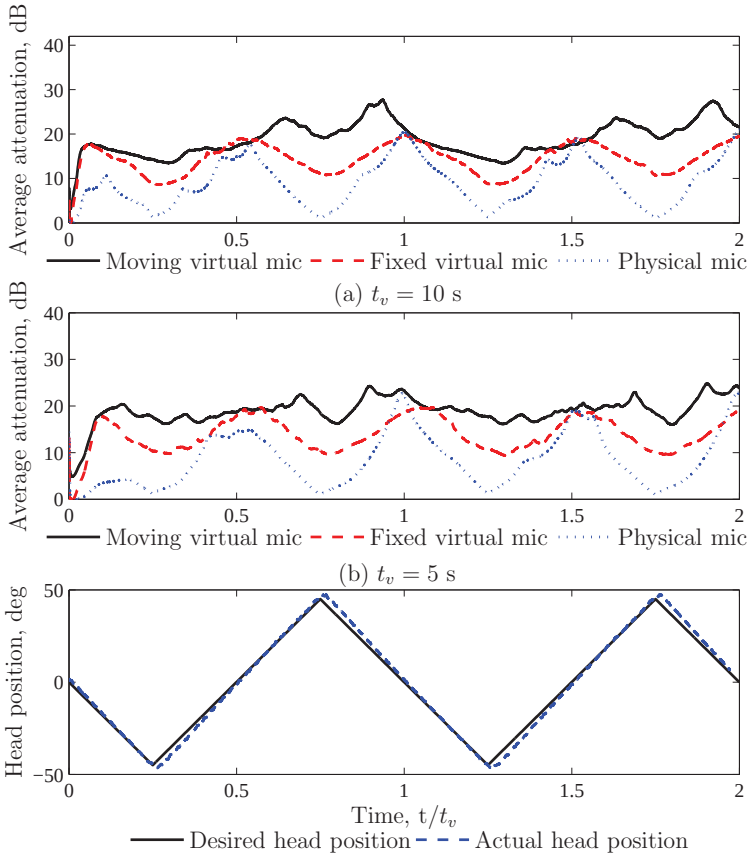

Figure 4.37: Tonal attenuation achieved off resonance at 510 Hz with the SOTDF moving virtual sensing method for a three-dimensional sound field using the measured pressures at three points (physical sensor arrangement shown in Fig. 4.8). Control profiles are shown for active noise control at the moving virtual microphone, a virtual microphone spatially fixed at $\theta = 0°$, and the physical microphone, for a period of rotation (a) $t_v = 10$ s; (b) $t_v = 5$ s; and (c) head position.

Table 4.6 gives the time average and standard deviation of the attenuation achieved at the moving virtual location when the virtual error signals are estimated using the measured pressures at three points. Tabulated results are given for active noise control at the moving virtual microphone, a fixed virtual microphone located at the ear of the artificial head when $\theta_h = 0°$, and the fixed physical microphone. Off resonance, Table 4.6 shows that active noise control at the moving virtual microphone provides up to an additional 5.8 dB of attenuation at the moving virtual location compared to active noise control at the fixed virtual microphone. Minimising the moving virtual error signal achieves up to an additional 12.6

Table 4.6: Time average and standard deviation (in parentheses) of the attenuation in dB achieved at the moving virtual location with the SOTDF moving virtual sensing method for a three-dimensional sound field when the measured pressures at three points are used to estimate the virtual error signals. Tabulated results are given for active noise control at the moving virtual microphone with the adaptive LMS moving virtual microphone technique, a fixed virtual microphone located at the ear of the artificial head when $\theta = 0°$ and the physical microphone.

t_v s	525 Hz			510 Hz		
	Moving virtual mic	Fixed virtual mic	Physical mic	Moving virtual mic	Fixed virtual mic	Physical mic
10	23.9(2.8)	17.6(3.4)	9.1(4.3)	21.5(3.8)	15.7(4.1)	8.9(5.2)
5	22.7(3.2)	17.2(3.5)	7.1(4.8)	18.9(3.9)	17.1(4.2)	8.3(5.7)

dB of attenuation at the moving virtual location compared to minimising the fixed physical error signal.

As expected, comparing Figs. 4.27 and 4.37 and the average attenuations achieved at the two excitation frequencies in Table 4.6 demonstrates that reduced control performance is achieved off resonance. As previously stated, this is because a number of modes contribute to the cavity response when the primary noise disturbance is off resonance. Table 4.6 also confirms that as the period of head rotation decreases, the average attenuation achieved at the moving virtual location decreases and the standard deviation increases. Again, this is because it takes a finite time for the controlled sound field to stabilise, so once the period of head rotation nears the reverberation time of the cavity, the control performance is compromised.

4.3.4 Results summary and comparison

The results of active noise control at the ear of the rotating artificial head with the three moving virtual sensing algorithms share a number of common features. Firstly, minimising the moving virtual error signal generated with either the remote moving microphone technique, the adaptive LMS moving virtual microphone technique or the SOTDF moving virtual sensing method generates the best control performance at the ear of the rotating artificial head. Experimental results therefore demonstrate that moving virtual sensors provide improved attenuation at the moving virtual location compared to either fixed virtual sensors or fixed physical sensors.

The experimental results obtained with each of the three moving virtual sensing

algorithms show that as the period of head rotation is reduced, the control performance reduces. This is because it takes a finite time for the controlled sound field to stabilise, so once the period of head rotation nears the reverberation time of the cavity, the control performance is compromised. A reduction in control performance was also seen off resonance when implementing any of the three moving virtual sensing methods. This is to be expected since several modes dominate the cavity response when the primary noise disturbance is off resonance.

Comparing Figs. 4.10 and 4.17, 4.11 and 4.22, and Tables 4.2 and 4.4 demonstrates that the remote moving microphone technique outperforms the adaptive LMS moving virtual microphone technique with $M_a = 4$ physical microphones in tetrahedral formation. The remote moving microphone technique estimates the error signal at the moving virtual location more accurately and generates greater attenuation at the moving virtual location compared to the adaptive LMS moving virtual microphone technique. Comparing Tables 4.2 and 4.4 shows that at resonance, up to an additional 4.2 dB of attenuation is achieved at the moving virtual location by employing the remote moving microphone technique instead of the adaptive LMS moving virtual microphone technique. Off resonance, implementing the remote moving microphone technique provides up to an additional 1.9 dB of attenuation at the moving virtual location compared to the adaptive LMS moving virtual microphone technique.

Comparing Tables 4.2 and 4.6 demonstrates that the SOTDF moving virtual sensing method is outperformed by the remote moving microphone technique in terms of the level of attenuation achieved at the moving virtual location. At resonance, up to an additional 5.8 dB of attenuation is achieved at the moving virtual location by employing the remote moving microphone technique instead of the SOTDF moving virtual sensing method. Off resonance, the remote moving microphone technique provides up to an additional 5.7 dB of attenuation at the moving virtual location compared to the SOTDF moving virtual sensing method. This improved control performance is achieved provided accurate measurement of the tonal transfer functions occurs in the preliminary identification stage of the remote moving microphone technique.

Although greater control is achieved at the moving virtual location with the remote moving microphone technique, the SOTDF moving virtual sensing method is much simpler to implement because it is a fixed scalar weighting method requiring only sensor position information. Also, the remote moving microphone technique is not robust to changes in the sound field that alter the transfer functions between

the error sensors and the sources, as was shown in Section 4.3.1.1. This moving virtual sensing method requires recalibration of the transfer functions between all the sources and the error sensors when any of the source or error sensor locations are altered. The SOTDF moving virtual sensing method is independent of the sensor and source locations within the sound field and the weight functions only need to be updated if the geometric arrangement of the physical and virtual locations changes with respect to each other. Comparing Tables 4.2 and 4.6 demonstrates that the SOTDF moving virtual sensing method outperforms the remote moving microphone technique when active noise control is performed in a modified sound field. At resonance in a modified sound field, up to an additional 5.8 dB of attenuation is achieved with the SOTDF moving virtual sensing method compared to the remote moving microphone technique. Off resonance in a modified sound field, the SOTDF moving virtual sensing method provides up to an additional 4.6 dB of attenuation at the moving virtual location compared to the remote moving microphone technique.

The SOTDF moving virtual sensing method is also outperformed by the adaptive LMS moving virtual microphone technique in an unmodified sound field. Comparing Tables 4.4 and 4.6 demonstrates that at resonance, the adaptive LMS moving virtual microphone technique provides up to an additional 1.3 dB of attenuation compared to the SOTDF moving virtual sensing method. Off resonance, up to an additional 5.2 dB of attenuation is achieved at the moving virtual location by employing the adaptive LMS moving virtual microphone technique instead of the SOTDF moving virtual sensing method. This improved control performance is achieved provided accurate measurement of the physical secondary transfer functions and the physical sensor weights occurs in the preliminary identification stage of the adaptive LMS moving virtual microphone technique.

Although greater attenuation is achieved at the moving virtual location with the adaptive LMS moving virtual microphone technique, the SOTDF moving virtual sensing method is much easier to implement, being a fixed scalar weighting method. Also, the adaptive LMS moving virtual microphone technique is not robust to changes in the sound field that may alter the transfer functions between the error sensors and the sources, as was shown in Section 4.3.2.1. As the SOTDF moving virtual sensing method is independent of the error sensor or source locations within the sound field it is robust to changes in the sound field adversely affecting the performance of the adaptive LMS moving virtual microphone technique. Comparing Tables 4.4 and 4.6 demonstrates that the SOTDF moving virtual sensing method outperforms the adaptive LMS moving virtual microphone technique when active

noise control is performed in a modified sound field. At resonance in a modified sound field, up to an additional 5.6 dB of attenuation is achieved with the SOTDF moving virtual sensing method compared to the adaptive LMS moving virtual microphone technique. Off resonance in a modified sound field, the SOTDF moving virtual sensing method provides up to an additional 4.4 dB of attenuation at the moving virtual location compared to the adaptive LMS moving virtual microphone technique.

4.4 Conclusion

In this chapter, a number of moving virtual sensing methods have been presented for three-dimensional sound fields. These moving virtual sensing algorithms create a zone of quiet capable of tracking a three-dimensional trajectory in a three-dimensional sound field. The moving virtual sensing algorithms developed in this chapter include the remote moving microphone technique, the adaptive LMS moving virtual microphone technique and the SOTDF moving virtual sensing method.

To determine the level of attenuation that can be expected at the ear of a human observer in practice, the performance of these moving virtual sensing algorithms in generating a moving zone of quiet at the single ear of a rotating artificial head has been experimentally investigated in a modally dense three-dimensional cavity. Results of real-time experiments demonstrated that moving virtual sensors provide improved attenuation at the moving virtual location compared to either fixed virtual sensors or fixed physical sensors.

The remote moving microphone technique for a three-dimensional sound field estimates the error signal at the moving virtual location by interpolating between the error signals at a number of spatially fixed virtual locations estimated using the remote microphone technique (Roure and Albarrazin, 1999). The remote moving microphone technique was shown to outperform the adaptive LMS moving virtual microphone technique and the SOTDF moving virtual sensing method in terms of the level of attenuation achieved at the ear of the rotating artificial head in real-time experiments. The remote moving microphone technique is, however, not robust to changes in the sound field that alter the transfer functions between the sources and the sensors.

The adaptive LMS moving virtual microphone technique for a three-dimensional sound field estimates the error signal at the moving virtual location as the sum of the weighted physical sensor signals at a number of physical microphones in an

array. In real-time experiments, four different configurations of physical microphones were investigated to determine which configuration results in the most accurate estimate of the moving virtual error signal. Arranging four physical microphones in tetrahedral formation was shown to estimate the moving virtual error signal most accurately and generated the greatest attenuation at the moving virtual location in real-time experiments. Like the remote moving microphone technique, the adaptive LMS moving virtual microphone technique was found to require recalibration of the transfer functions and the physical sensor weights if any of the error sensor or source locations are altered, or if the modal response of the cavity is changed.

The SOTDF moving virtual sensing method for a three-dimensional sound field estimates the error signal at the moving virtual location using diffuse field theory. In real-time experiments active noise control at the SOTDF moving virtual sensors was shown to provide improved attenuation at the ear of the rotating artificial head compared to either fixed virtual or fixed physical sensors in a modally dense sound field. This demonstrates that SOTDF moving and fixed virtual sensors are suitable for use in a sound field that is not perfectly diffuse. While greater control was achieved at the moving virtual location with the remote moving microphone technique and the adaptive LMS moving virtual microphone technique, the SOTDF moving virtual sensing method is much simpler to implement as it is a fixed weighting technique requiring only sensor position information. Also, unlike the remote moving microphone technique and the adaptive LMS moving virtual microphone technique, this moving virtual sensing method is robust to changes in the sound field that may alter the transfer functions between the error sensors and the sources.